processes

MDPI

Article

Thermal Performance Evaluation for Two Designs of Flat-Plate Solar Air Heater: An Experimental and CFD Investigations

Mahmoud S. El-Sebaey [1,*], Asko Ellman [2], Sh. Shams El-Din [1] and Fadl A. Essa [3]

[1] Mechanical Power Engineering Department, Faculty of Engineering, Menoufia University, Shebin El-Kom 32511, Egypt
[2] Faculty of Engineering and Natural Sciences, Tampere University, 33100 Tampere, Finland
[3] Mechanical Engineering Department, Faculty of Engineering, Kafrelsheikh University, Kafrelsheikh 33516, Egypt
* Correspondence: mahmoud.el-sebaey@sh-eng.menofia.edu.eg or eng_mahmoudelsebaey@yahoo.com

Abstract: The main objective of this research was to create two different configurations of a flat-plate solar air heater, namely, Conventional-Case A and Modified-Case B, and develop a three-dimensional computational fluid dynamics (CFD) model using ANSYS R15.0. The purpose of the CFD model was to simulate the heat transfer behavior of the proposed solar air heaters under unsteady conditions. The RNG k-ε turbulence model was employed for this CFD study. The experiments were conducted on sunny days, under the same conditions as the Egyptian climate. The results of the experiments show that the simulated CFD model and the measured outlet airflow temperatures, relative humidity, and velocities of the two tested solar air heaters were compared. The developed model made very satisfactory predictions. Moreover, the deviations between the average CFD outlet air temperatures and the experimental results were 7% and 7.8% for Case B and Case A, respectively. The CFD-simulated average relative humidity was reduced by 31.6% when using Case B compared with Case A, and it was reduced by 28.8% when comparing the experimental data to Case B. Additionally, the average CFD thermal efficiencies obtained for Case B and Case A were 28.7% and 21.6%, respectively, while the average experimental thermal efficiencies for the cases were 26.4% and 18.2%, respectively. The proposed model can be used to design and simulate other solar air heater designs.

Keywords: solar air heaters; natural convection; air gap; CFD modeling and thermal efficiency

Citation: El-Sebaey, M.S.; Ellman, A.; El-Din, S.S.; Essa, F.A. Thermal Performance Evaluation for Two Designs of Flat-Plate Solar Air Heater: An Experimental and CFD Investigations. *Processes* **2023**, *11*, 1227. https://doi.org/10.3390/pr11041227

Academic Editors: Omar Dario Lopez Mejia and Santiago Lain

Received: 8 March 2023
Revised: 11 April 2023
Accepted: 14 April 2023
Published: 16 April 2023

1. Introduction

Solar energy has a beneficial effect on the development of sustainable and clean energy sources [1]. However, although heating accounts for a significant portion of the global energy consumption, it is given less attention compared to other sectors [2]. Among the solar energy harvesting methods available, solar air heaters (SAHs) are widely recognized as a cost-effective option for various purposes, including drying [3], room heating, and industrial activities [4].

An SAH acts as a solar thermal collector that captures thermal solar energy and converts it into warm air suitable for low-temperature residential and industrial applications [5]. As the energy demand continues to increase, with conditioning systems accounting for a significant portion, SAHs could play a crucial role in reducing the energy consumption of buildings. Conventional SAHs have been widely adopted worldwide for solar thermal processes [6]. Due to its simple design, affordability, and low maintenance costs, the SAH is an ideal choice for various applications, including heating, dehumidification, building heating, energy storage, and drying agricultural products [7].

The thermal efficiency of an SAH is a crucial factor to consider when evaluating its performance [8]. However, the coefficient of heat transfer between the absorber and the airflow inside the SAH is low due to the thermo-physical properties of the airflow, a major weakness that poses a significant limitation in the development of SAHs [9]. In an effort to

enhance efficiency and cost-effectiveness, researchers have conducted numerous studies over the years to increase the heat transfer coefficient [10]. A flat-plate solar air heater (FPSAH) is a type of heat exchanger that converts radiated solar energy into heat [11].

Researchers have introduced various approaches to improve the heat transfer coefficient of SAHs, including modifying their shape. For instance, rectangular [12], triangular [13], curved, spiral, corrugated, and circular absorber plates have been investigated [14].

Several studies have investigated the positioning of the absorber plate with respect to the airflow to improve the heat transfer in SAHs [15–17]. Additionally, the addition of baffles or fins has been explored as means of enhancing the heat transfer rate between the absorber plate and the air [18,19].

Researchers have also explored alternative absorber shapes, such as U-shaped corrugation or V-shaped grooves, to enhance the efficiency of SAHs [20]. These studies have demonstrated that the absorber position and air retention time in the collector are crucial factors in improving the efficiency of the system. However, conducting experiments to determine these factors can be time-consuming and expensive. Therefore, modeling and simulation tools have been utilized to address these issues.

Sanjay and colleagues [21] utilized CFD to develop a model of an SAH with rib roughening, examining how different rib arrangements affect the frictional loss and heat transfer properties. Meanwhile, using ANSYS Fluent, Dongxu et al. [22] employed numerical methods to investigate heat transfer in a roughened SAH featuring multiple V-shaped ribs on the absorber plate. Espinosa et al. [23] developed a numerical model of an SAH to estimate its thermal efficiency.

The literature reviewed lacks sufficient articles on simulating a flat-plate solar air heater (FPSAH) using ANSYS Fluent, and there was limited discussion on choosing models that accurately predict the mode and dynamics of heat transfer. This study aims to fill this gap by identifying the required boundary conditions, thermo-physical material and fluid properties, and meteorological conditions to create an accurate ANSYS Fluent model to simulate the FPSAH, which has not been previously explored. Thus, the primary aim of this research is to:

1. Perform experimental investigations on two FPSAH designs under the weather conditions in Shebin El-Kom, Egypt.
2. Evaluate the influence of operating parameters on the thermal performance of the tested FPSAH designs.
3. Create a detailed and dynamic CFD model capable of accurately simulating the real-world operation of FPSAHs under realistic operating conditions.

2. Test Rig Description

A schematic view of a conventional FPSAH (Case A) is presented in Figure 1. The heart of the FPSAH, which is the absorber, was made of a 1 mm galvanized iron sheet with dimensions of 1000 mm × 2000 mm, which was later painted black. The incoming solar radiation penetrates a 3 mm glass plate with the same dimensions as the absorber, with a distance of 100 mm between them. The air enters the solar air heater at a low temperature, and the absorber then transfers the maximum amount of heat to the airflow so that the outlet temperature reaches its maximum value. To minimize the heat lost to the atmosphere, the absorber bottom wall was insulated with 100 mm of sawdust. The device had a tilt angle of 30°, measured from the horizontal in the city of Shebin El-Kom, Egypt, which is located at 30.56° N and 31.00° E. Similar to Case A, Case B refers to a modified FPSAH using an air gap, as indicated in Figure 2. The gap between the two glass layers was 50 mm, with static air to raise the efficiency of the SAH. All the side walls of the upper glass box were glass with a thickness of 3 mm.

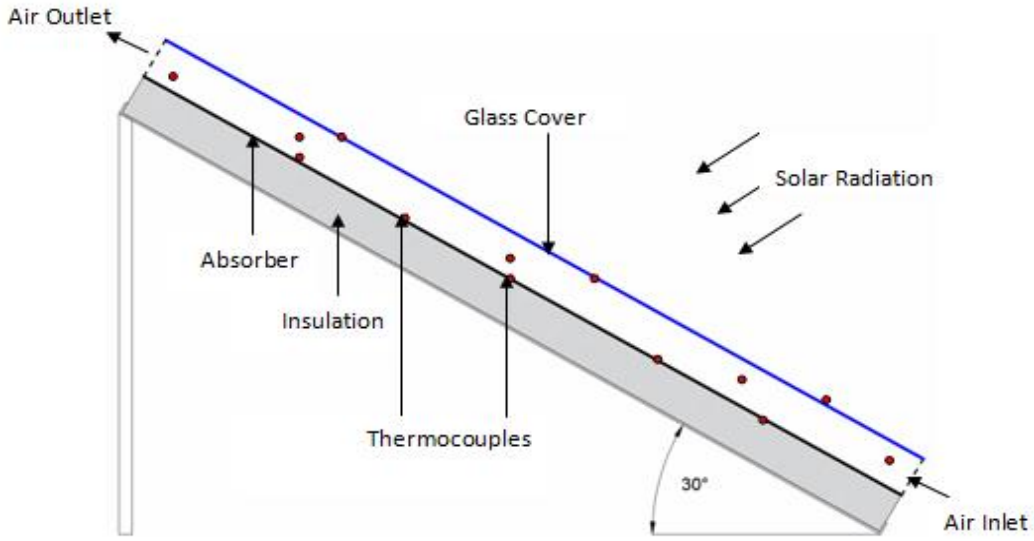

Figure 1. A schematic view of the conventional FPSAH, Case A.

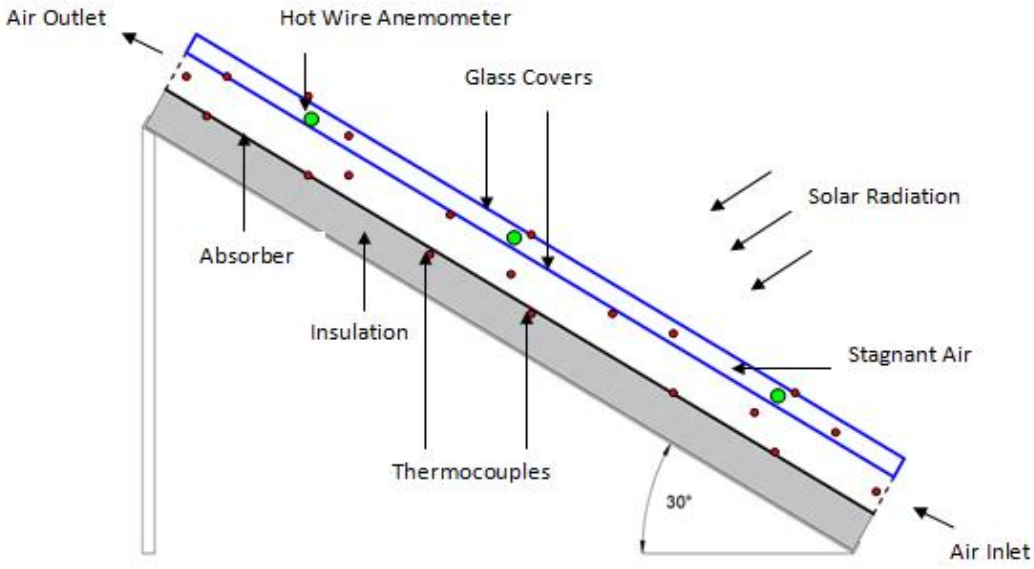

Figure 2. A schematic view of the Modified FPSAH, Case B.

Figure 3 exhibits a photograph of the test rig. The two tested FPSAHs (Case A and Case B) were orientated in a southern direction to receive the most global irradiation through the experiments.

The two tested devices were equipped with a set of calibrated K-type thermocouples (range of −210 to +750 °C; accuracy of ±1 °C; uncertainty of 1.3%) to measure the temperature over time. The thermocouples were installed on each inlet, outlet, absorber, glass, and side walls at different points to record the average values of the temperatures. A calibrated digital pyranometer was used to measure the amount of global irradiation (range of 0 to 2000 W/m^2; accuracy of ±10 W/m^2; uncertainty v1.6%). Additionally, a calibrated hot-wire anemometer was utilized to measure the inside velocity of the airflow at different positions along the two tested solar air heaters (range of 0 to 25 m/s; accuracy of ±0.1 m/s; uncertainty of 1.2%).

Case A

Case B

Figure 3. A photograph of the two FPSAH designs.

3. Thermal Analysis

3.1. Energy Balance

The energy balance of each part of the two tested solar air heaters {Case A and Case B} can be established. The energy balance of each part can be obtained using the classical method. In the chosen part, the total amount of the thermal flux can be written as the sum of all exchanged energy among the parts and the amount of solar energy lost or gained by this part. The thermal flux developed for each case of the solar air heater designed was described as follows:

3.1.1. Conventional Solar Air Heater (Case A)

In case A, the airflow absorbs a portion of global irradiation transmitted through the glass cover and then exchanges energy within both the flat-plate absorber and the glass cover by convection, thus:

$$S_Q = \frac{1}{S.L}\left[A_{gc}\tau_{gc}\alpha_f I(t) + A_{ab}h_{cf-ab}(T_{ab} - T_f) + A_{gc}h_{cf-gc}(T_{gc} - T_f)\right] \quad (1)$$

Glass Cover

A portion of global solar energy is absorbed by the glass cover, which exchanges energy with both the ambient air and airflow by convection and with both the flat-plate absorber and the sky by radiation, thus:

$$\frac{m_{gc}c_{pgc}}{A_{gc}}\frac{\partial T_{gc}}{\partial t} = \alpha_{gc}I(t) + h_{cex}\left(T_{amb} - T_{gc}\right) + h_{cf-gc}\left(T_f - T_{gc}\right) + h_{rgc-bb}\left(T_{ab} - T_{gc}\right) + h_{rgc-sky}\left(T_{sky} - T_{gc}\right) \quad (2)$$

Absorber Plate

The flat-plate absorber absorbs a portion of the transmitted global solar energy via airflow and the glass cover and exchanges energy with the airflow through convection, with the glass cover through radiation, and with the insulation by conduction, thus:

$$\frac{m_{ab}c_{pab}}{A_{ab}}\frac{\partial T_{ab}}{\partial t} = \tau_{gc}\tau_f\alpha_{ab}I(t) + h_{cf-ab}\left(T_f - T_{ab}\right) + h_{rab-gc}\left(T_{gc} - T_{ab}\right) + U_{cond}\left(T_{Ins} - T_{ab}\right) \quad (3)$$

3.1.2. Modified Solar Air Heater (Case B)

In Case B, the airflow partially absorbs the solar radiation, which is transferred by the two glass covers, the stagnant air, and the energy exchanged through convection between the SAH's absorber and the lower glass cover, thus:

$$S_Q = \frac{1}{S.L}\left[A_{gc}\tau_{st}{\tau_{gc}}^2\alpha_f I(t) + A_{ab}h_{cf-ab}\left(T_{ab} - T_f\right) + A_{gc}h_{cf-gc2}\left(T_{gc2} - T_f\right)\right] \quad (4)$$

Upper Glass Cover

The upper glass cover absorbs a portion of solar irradiation, exchanges the energy with the ambient air through convection, then with the stagnant air, and with the lower cover of the glass and with the sky through radiation, thus:

$$\frac{m_{gc}c_{pgc}}{A_{gc}}\frac{\partial T_{gcu}}{\partial t} = \alpha_{gc}I(t) + h_{cex}\left(T_{amb} - T_{gcu}\right) + h_{cgcu-st}\left(T_{st} - T_{gcu}\right) + h_{rgcu-gcl}\left(T_{gcl} - T_{gcu}\right) + h_{rgcu-sky}\left(T_{sky} - T_{gcu}\right) \quad (5)$$

Stagnant Air

A portion of the global irradiation transmitted by the upper glass cover is absorbed by the stagnant air, which then exchanges energy with the lower glass cover by convection, thus:

$$\frac{m_{st}c_{pst}}{A_{gc}}\frac{\partial T_{st}}{\partial t} = \alpha_{st}\tau_{gc}I(t) + h_{cgcl-st}\left(T_{gcl} - T_{st}\right) + h_{cgcu-st}\left(T_{gcu} - T_{st}\right) \quad (6)$$

Lower Glass Cover

The lower glass cover absorbs a portion of the global solar energy transmitted by the upper glass cover and the stagnant air and exchanges energy with the stagnant air and the airflow by convection. In addition, it exchanges energy with the absorber flat-plate and the upper glass cover by radiation, thus:

$$\frac{m_{gc}c_{pgc}}{A_{gc}}\frac{\partial T_{gcu}}{\partial t} = \alpha_{gc}\tau_{gc}\tau_{st}I(t) + h_{cgcl-st}\left(T_{st} - T_{gcl}\right) + h_{cf-gcl}\left(T_f - T_{gcl}\right) + h_{rgcl-ab}\left(T_{ab} - T_{gcl}\right) + h_{rgcl-gcu}\left(T_{gcu} - T_{gcl}\right) \quad (7)$$

Absorber Plate

The flat-plate absorber absorbs a portion of the transmitted global irradiation through the stagnant air and the two glass covers and exchanges energy with the airflow by convection and with the lower glass cover by radiation and conduction from the insulation, thus:

$$\frac{m_{ab}c_{pab}}{A_{ab}}\frac{\partial T_{ab}}{\partial t} = {\tau_{gc}}^2\tau_{st}\tau_f\alpha_{ab}I(t) + h_{cf-ab}\left(T_f - T_{ab}\right) + h_{rab-gcl}\left(T_{gcl} - T_{ab}\right) + U_{cond}\left(T_{Ins} - T_{ab}\right) \quad (8)$$

3.2. Calculation of the Relative Humidity

The relative humidity of the airflow though the FPSAH can be calculated as [24]:

$$RH = \frac{e_w - N(1 + 0.00115T_w)(T_d - T_w)}{e_d} \times 100 \quad (9)$$

where T_d and T_w are the dry and wet bulb temperatures, in °C.

N is a constant equal to 0.6687451584.

$$e_w = 6.112e^{\left(\frac{17.502T_w}{240.97+T_w}\right)} \quad (10)$$

$$e_d = 6.112e^{\left(\frac{17.502T_d}{240.97+T_d}\right)} \quad (11)$$

3.3. Thermal Efficiency

The thermal efficiency of the FPSAH can be calculated as [25]:

$$\eta_{th} = \frac{\dot{m}C_{pf}\left(T_{f_{out}} - T_{f_{int}}\right)}{A_{gc}I(t)} \quad (12)$$

The specific heat of the air is provided by:

$$C_{pf} = 1009.26 - 0.0040403T_f - 6.1759 \times 10^{-4}{T_f}^2 - 4.097 \times 10^{-7}{T_f}^3 \quad (13)$$

T_f is in °C.

4. Economic Analysis

An economic analysis presents the performance of the FPSAH in terms of its cost and benefits. The results of this analysis assist in selecting an appropriate device for any specific type of application. The heating levelized cost (HLC) was the parameter utilized to estimate the cost per kWh by considering key factors such as the capital cost, operating cost, maintenance cost, lifetime, inflation rate, and the device efficiency, etc. The HLC is estimated using the following equation [26]:

$$HLC = \frac{AC}{AE} \quad (14)$$

where AE is the average annual energy produced by the collector, while AC represents the total annual cost for the collector and can be calculated as:

$$AC = FC + MC + OC - SF \quad (15)$$

The fixed annual cost (FC) is determined by:

$$FC = CF.CC \quad (16)$$

where CC is the capital cost of the collector, and CF is the capital recovery factor, which can be calculated as:

$$CF = \frac{i.(1+i)^n}{(1+i)^n - 1} \quad (17)$$

where n is the economic collector lifetime.

The annual maintenance cost (MC) per year is determined using:

$$MC = (0.15).FC \quad (18)$$

The annual savage factor (SF) is determined by:

$$SF = FF.S \tag{19}$$

$$FF = \frac{i}{(1+i)^n - 1} \tag{20}$$

$$S = (0.2).CC \tag{21}$$

where i is the annual interest rate, %.

5. Computational Fluid Dynamics (CFD)

CFD is a computer code that can predict and explain the phenomena associated with heat, mass, flow, and energy, such as fluid flow, heat transfer, chemical reaction, etc., involving numerical solutions of the conservation equations for energy, mass, and momentum.

5.1. Geometry Creation and Details of the Meshing

In any problem, the initial step in CFD is the creation of a geometric model. Three-dimensional geometries of Case A and Case B were created using the ANSYS R15.0 Workbench, which provided Design Modeller as a design tool to develop the geometric configurations of the physical problem domain. Figure 4 presents the geometric configurations of both tested SAHs with similar dimensions to the designed experimental configurations, which were imported into the ANSYS meshing module.

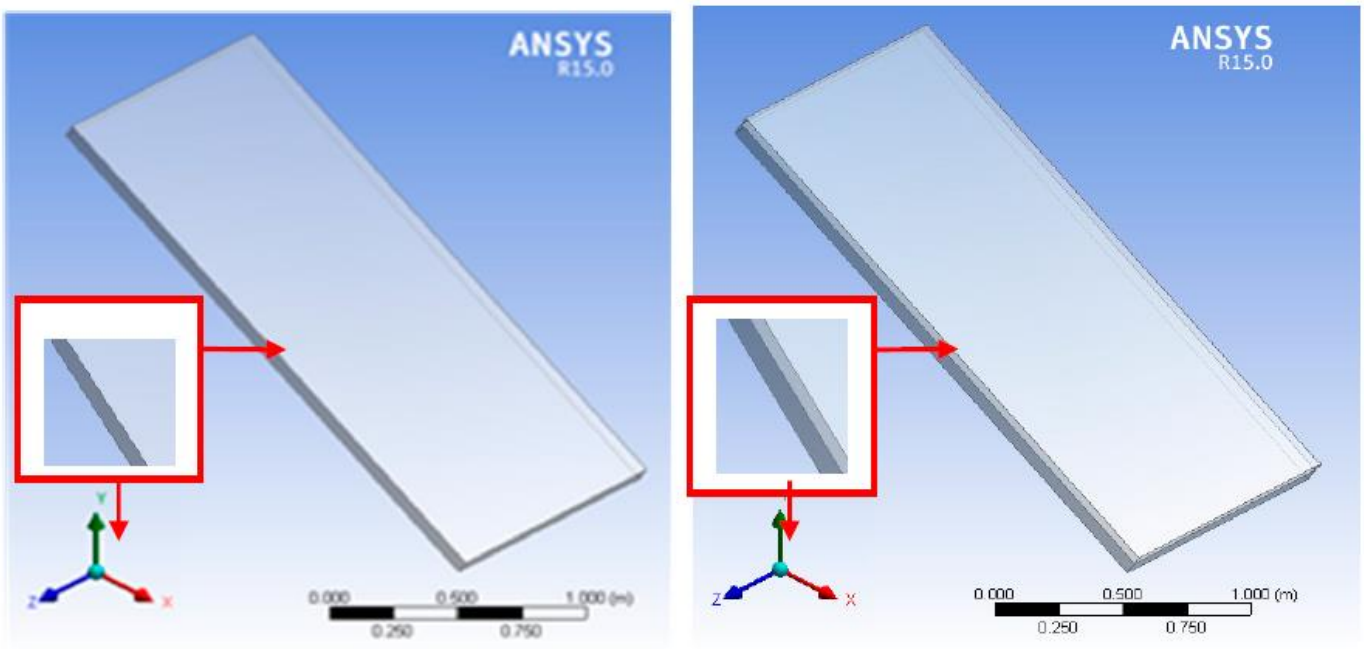

(Case A) (Case B)

Figure 4. Geometric model for the two tested FPSAHs.

Since the geometries of Case A and Case B did not involve any type of curved surfaces, the CutCell meshing method was extremely well-suited [27,28] and could provide accurate solutions with the moderate computational time required to use the ANSYS MESHING workbench, as shown in Figure 5. The total number of nodes for Case A and Case B in the meshed domain was 218,160 and 366,226, respectively, and the total number of nodes for the elements was 206,400 and 343,600, respectively.

After the mesh generation, it was important to assess its quality as it can influence the solution accuracy to a great extent. There were various available parameters in ANSYS for assessing the mesh quality. Several of these important parameters were skewness, aspect ratio, and element quality. In this research, some of these parameters were studied and analyzed. From the survey, the average skewness value should be permanently less than 0.3 for a perfect mesh quality. Therefore, it is important to note that all of the elements had skewness values of less than 0.1 for both the solar air heaters tested. Similarly, the aspect ratio parameter was estimated for the generated mesh quality. The average aspect ratio value for a good quality of mesh should be less than 2. All the elements had an aspect ratio value of less than 1.2. These results show that the mesh, which was generated with mostly hexahedral elements, was a perfect quality mesh for the skewness and aspect ratio.

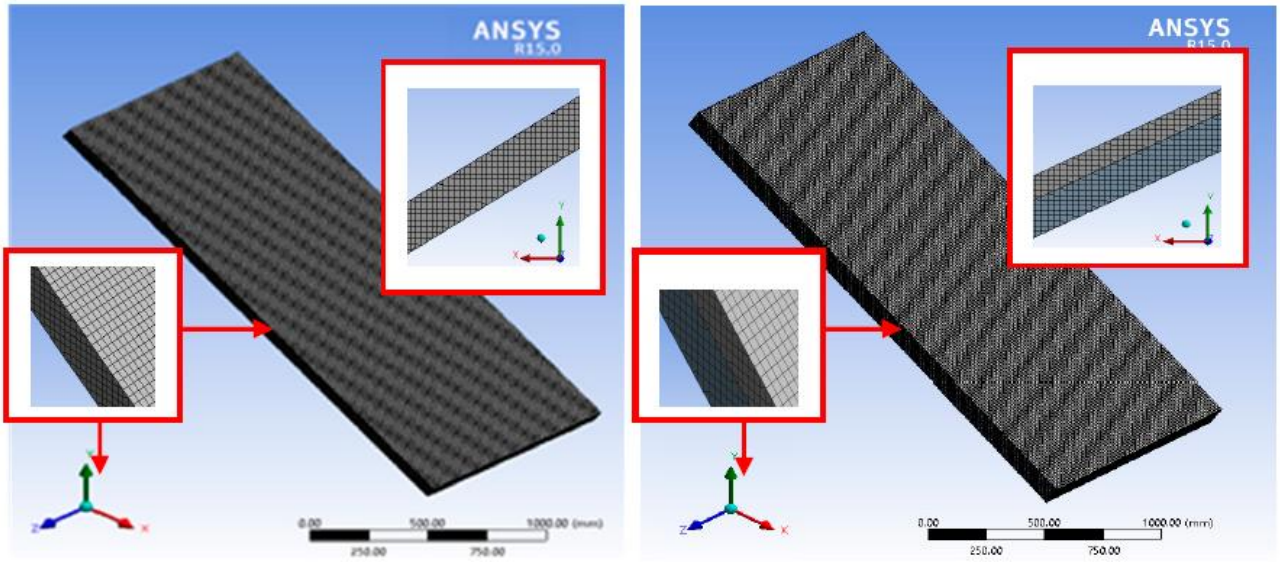

Case A Case B

Figure 5. Meshed CFD domain for the two tested FPSAHs.

5.2. Assumptions for Simulation

This type of solution requires some assumptions to simplify the complicated flow geometries, such as solar air heater problems, with a small error value compared to the exact solutions. The following assumptions were considered here for the CFD simulation modeling:

1. As the surrounding air velocities were very low, the influence of the surrounding air velocity was neglected, and free convection was assumed.
2. The bottom of the physical absorber of the system was insulated and was therefore considered adiabatic.
3. As the variation in temperatures was medium, the air properties, such as the thermal conductivity, specific heat, viscosity, and density, were assumed to be piecewise linear, and the temperature and the physical properties of the solid materials were assumed to be constants.
4. The pressure of the outlet air was assumed to be equal to the atmospheric pressure.

5.3. Governing Equations

5.3.1. Mass Conservation Equation

The equation of mass conservation or the continuity equation can be expressed as the following as within a controlled volume, the mass of the flow remains constant with time:

$$\frac{\partial \rho}{\partial t} + \nabla . \left(\rho \vec{V} \right) = 0 \tag{22}$$

where $\vec{V}$ is the overall velocity vector, and ρ is the density.

5.3.2. Momentum Conservation Equation

The change in momentum over time is equal to the sum of the force acting on the system. This Navier–Stokes equation is reflective of the law of conservation of momentum, and it can be expressed as:

$$\frac{\partial}{\partial t} \left(\rho \vec{V} \right) + \nabla . \left(\rho \vec{V} \vec{V} \right) = -\nabla p + \nabla . \bar{\bar{\tau}} + \rho \vec{g} \tag{23}$$

where $\rho \vec{g}$ is the gravitational body force, and $\bar{\bar{\tau}}$ is the viscous stress, which is given by:

$$\bar{\bar{\tau}} = \mu \left[\left(\nabla \vec{V} + \nabla \vec{V}^{T} \right) - \frac{2}{3} \nabla . \vec{V} I \right] \tag{24}$$

5.3.3. Energy Equation

Similarly, the first law of thermodynamics reflects the Navier–Stokes energy equation. The energy conservation law states that the total energy of the system equals the sum of work and heat added to the system.

$$\nabla . (\vec{V} (\rho E + P)) = \nabla . (K_{eff} \nabla T - \sum\nolimits_{j} h_j . \vec{j}_j + (\bar{\bar{\tau}}_{eff} . \vec{V})) \tag{25}$$

where K_{eff} is the effective conductivity and can be provided by:

$$K_{eff} = k + \frac{c_{pf} \mu_t}{Pr_t} \tag{26}$$

5.4. Boundary Types and Conditions for the Two Tested FPSAH Models

Defining appropriate boundary types and boundary conditions is important to achieving an exact solution for any fluid flow problem. The chosen boundary conditions were a significant stage in the CFD simulation. Any CFD model solves the different equations included in the model based on constraints. The physical or real boundary conditions were simplified and idealized to insert them into the CFD simulation. For example, in this research, the FPSAH bottom, which was insulated physically, was considered to have an adiabatic wall as a boundary condition in the simulation setup. For the inlet and outlet portions, the boundary conditions were taken into account for velocity inlet and pressure outlet. Table 1 indicates the boundary types and conditions for the various parts of the two tested solar air heaters. The description of the upper glass covers and side walls, which were made from transparent window glass, assumed that they were semi-transparent walls, as provided in the CFD setup. Due to the convection heat transfer between the surrounding ambient air and the upper glass cover and side walls, the thermal conditions were assumed to be a convection of 5.7 $W/m^2.k$ from the empirical correlation of zero wind velocity. In addition, the boundary conditions for the inlet of the FPSAHs was assumed to be a velocity inlet with an average value of 1 m/s, and a gauge pressure of zero value was assumed for the outlet boundary condition.

Table 1. Boundary types and conditions for FPSAHs models.

Zone Name	Zone Type	Description	Thermal Conditions	Wall Thickness
Upper Glass Wall	Wall	Semi-Transparent T: 0.89- R: 0.08-A:0.03	Convection (5.7 $W/m^2 \cdot K$) And Radition	0.003 m
Lower Glass Wall	Wall	Semi-Transparent T: 0.89- R: 0.08-A:0.03	Coupled	0.003 m
Absorber Wall	Wall	Opaque	Convection (9.5 $W/m^2 \cdot K$) And Radition	0.001 m
Side Walls	Walls	Semi-Transparent T: 0.89- R: 0.08-A:0.03	Convection (5.7 $W/m^2.k$)	0.003 m
Inlet	Velocity Inlet	1 m/s		
Outlet	Pressure Outlet	Gauge Pressure 0 kPa		

where T, R, and A are the transmissivity, reflectivity, and absorption coefficients of glass, respectively.

5.5. Models Selection for Simulation

The operating parameters and models utilized in the simulation of Case A and Case B for the two tested FPSAHs in the FLUENT ANSYS solver are indicated in Table 2. After fixing the required input parameters and models, the solution was initialized. The time step was initiated at 0.001 s and reached 5.0 s, according to the ease of time and convergence needed to complete the solution of the simulation.

Table 2. Input parameters and models of the solver.

Function	Specification		
Solver Setting	Space	3D	
	Time	Unsteady; first-order implicit	
	Viscous Model	Turbulence model; k-epsilon with RNG Enhanced wall treatment with thermal effects	
	Radiation	Rosseland radiation model with solar loading and solar ray tracing Utilizing solar calculator (latitude 30.5° N and longitude 31.01° E) Days: 14:16.06.2022 Start time: 07.00 AM to End time: 07.00 PM North and West directions of the SAH	
Material Properties	Solid	Glass and Galvanized iron	Thermo-physical properties including: density; thermal conductivity; specific heat capacity
	Fluid	Air	
Operating Conditions	Operating Pressure	101.3 kPa	
	Gravity	−9.81 Z-Direction	
	Operating Temperature	288.16 K	

6. Results and Discussion

The performance of the flat-plate solar air heaters was influenced directly by the weather conditions, especially the ambient temperature, global irradiance, and wind speed. Figure 6 shows the average values of the minimum and maximum ambient air temperature for Shebin El-Kom city, Egypt during the year. The high values were obtained during the months of June and August. In the year under review, temperatures were low from November to February. However, the global irradiance intensity increased with an increase in temperature from March to October. Thus, it is possible to employ solar air heating in Shebin El-Kom during this period. Therefore, the experimental tests were conducted on

sunny days from 14–16 June 2022. Figure 7 shows the hourly variations in the experimental and CFD data for global irradiance as well as the ambient temperature and the ambient relative humidity for the different sunny days tested. It can be seen from Figure 7 that the results indicate a good agreement and similar trends between the CFD-simulated results and measured data for the intensity of the solar global irradiance all over the tested days (with maximum amounts of discrepancy of 7%). It can also be noted that the CFD-simulated and experimental global irradiance increased gradually through the local daytime and reached peak values at 12:00, after which they decreased according to the weather conditions. In addition, the variations in the ambient air temperature during the day ranged between 18 °C at night and 38 °C during the day. Figure 8 shows the variations in the ambient air velocity throughout the daytime period of the tested sunny days; the ambient velocities fluctuated between increment and decrement. According to Figure 8, the minimum and maximum ambient velocity during the tested days ranged between 0.25 and 3.2 m/s, respectively.

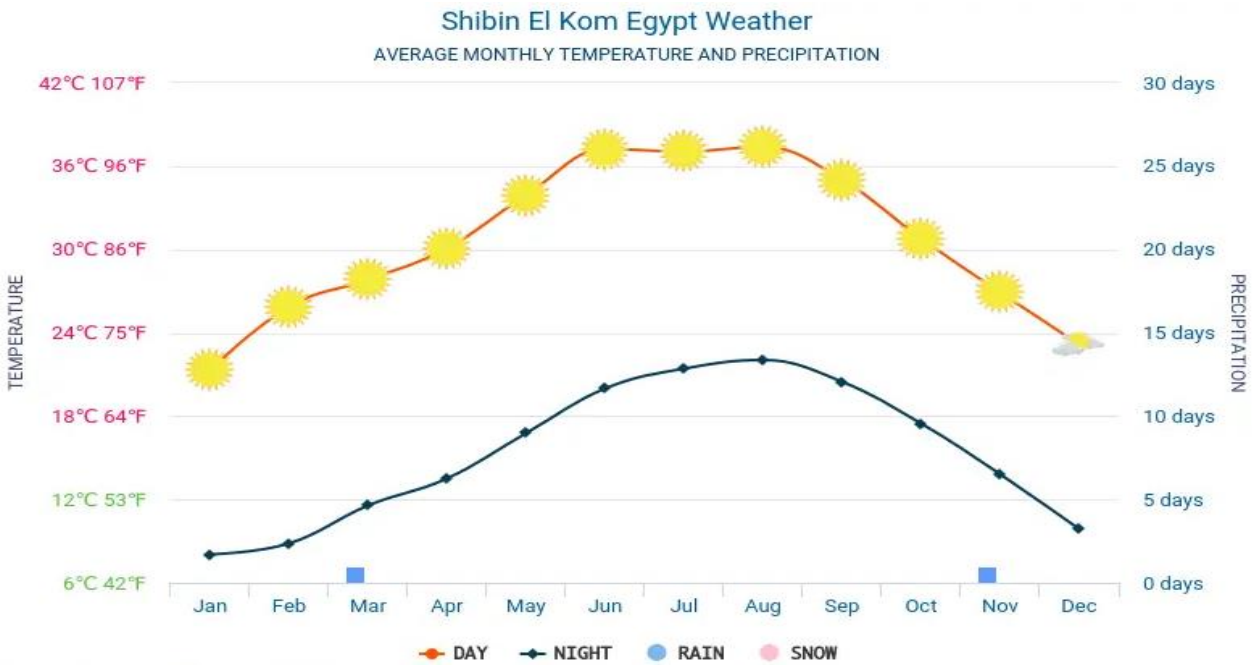

Figure 6. Variations in average values of the minimum and maximum temperatures of the ambient air for Shebin El-Kom city, Egypt during the year.

In the FPSAHs, the temperature of the absorber, the outlet air flow, glass covers, the interior of the air gab, and the stagnant air play a pivotal role in the FPSAH's performance. In general, the effectiveness of the FPSAH depends on the difference in temperature between the absorber and glass cover, as well as the difference in temperature between the inlet and outlet airflows.

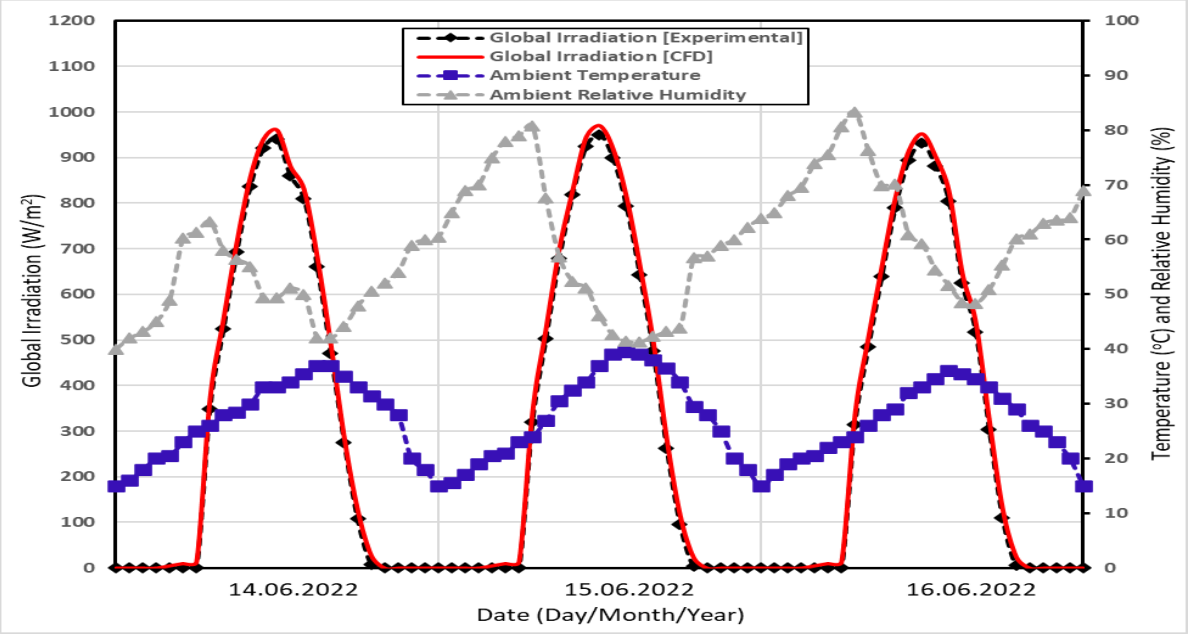

Figure 7. Variations in global irradiance, temperature, and relative humidity of ambient air during experiments.

The variations in the measured temperatures of the absorber, gab, glass covers, stagnation air, inlet, and outlet airflow during the tested sunny days for the two tested solar air heater configurations are indicated in Figure 9. From this Figure, it can clearly be seen that the temperatures of the absorber and outlet airflow for Case B are higher when compared with the temperatures of the absorber and outlet airflow in Case A. Thus, the presence of stagnant air near each absorber plate is important in raising the thermal efficiency of the FPSAH. In addition, it can clearly be seen from Figure 9 that the maximum absorber temperatures obtained at 13:00 ranged between 76 and 73.5 °C for Case B and ranged between 70.3 and 63.7 °C for Case A during the tested days.

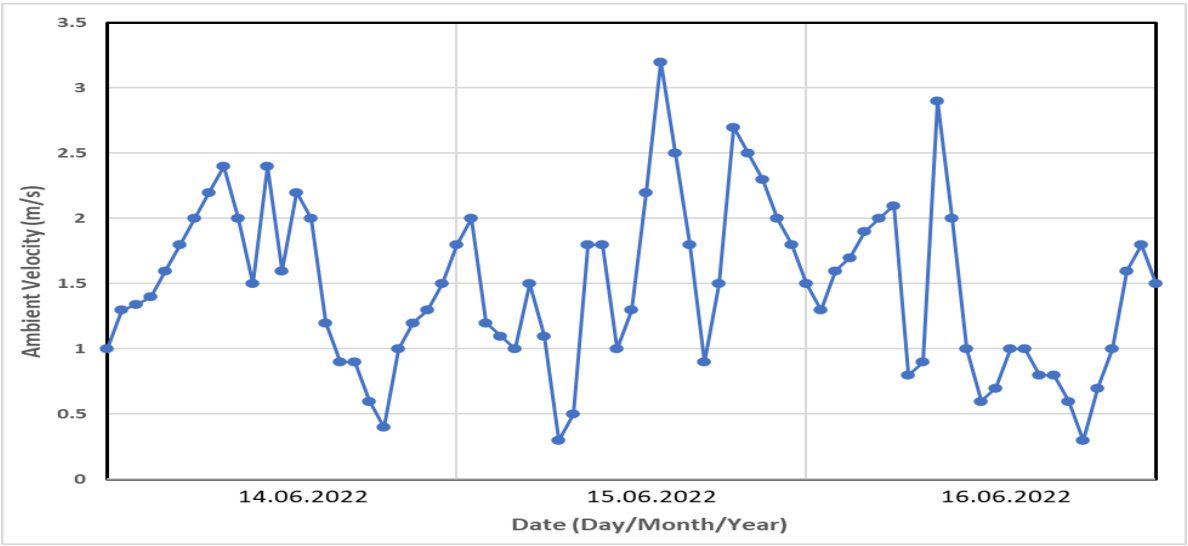

Figure 8. Variations in ambient air velocities during experiments.

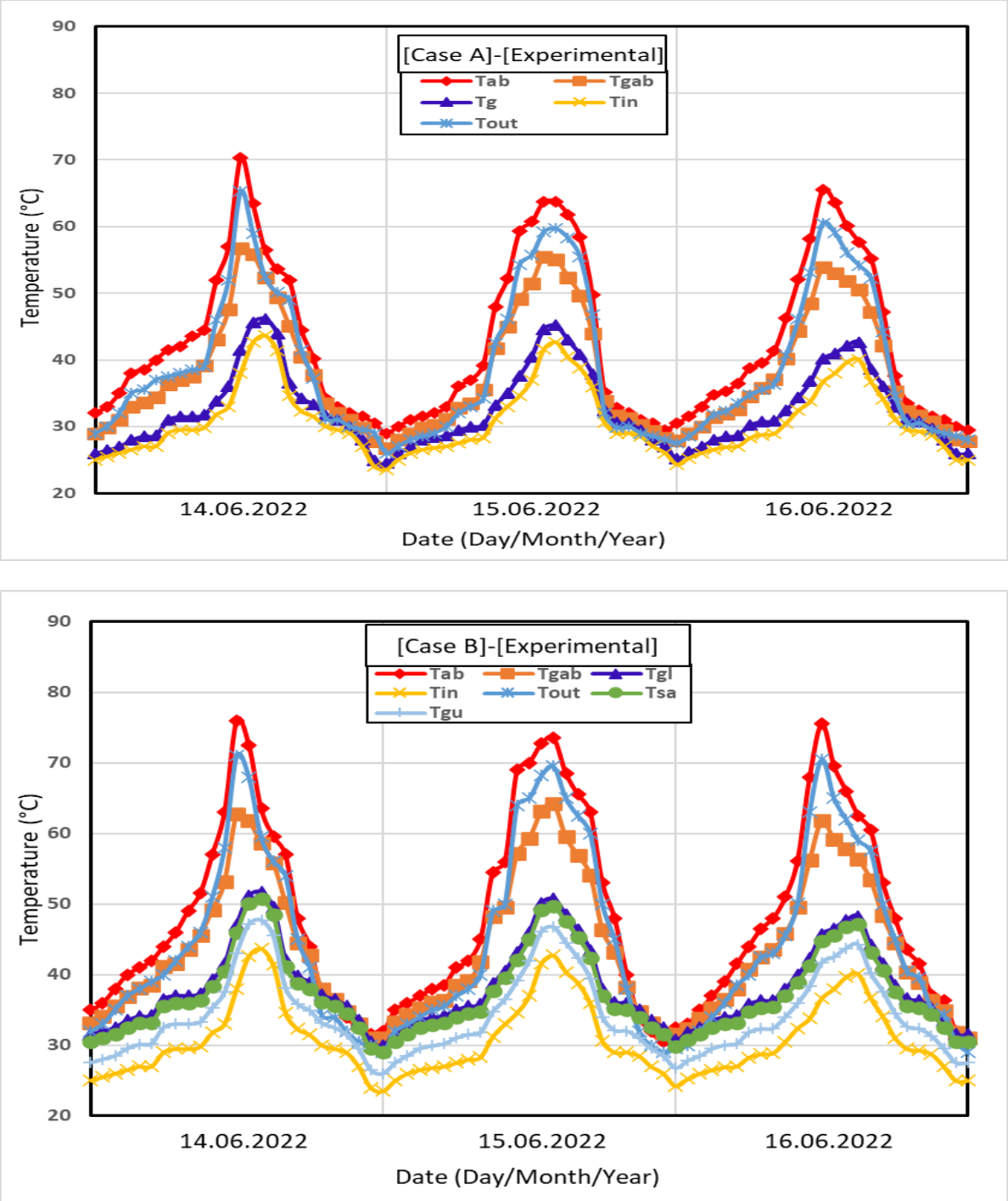

Figure 9. Temperature evolution of the components and the two tested FPSAHs.

The temperature contours for the absorber and upper glass cover for both tested Case A and Case B at different time intervals on 15 June 2022 are shown in Figures 10 and 11, respectively. The coding color for the temperatures is shown in the charts in Kelvin. The color "blue" shows the minimum temperature values, and the color "red" indicates the maximum temperature values. The temperature contour charts of the flat-plate absorber and the upper glass cover suggest that:

- Inside the both tested solar air heaters, the temperatures of the flat-plate absorber and upper glass cover begin to increase as global solar irradiation falls on the SAH. The

temperature contours show increments of gradual increase until 14:00; after this point, they decrease steadily.

- Within the tested FPSAH models, the airflow temperature begins to increase as the global irradiation falls on the absorber. After some time, the air flow begins to heat up, and the density of the airflow decreases, leading to an increase in the velocity of the airflow. The interior airflow temperatures inside both tested air heaters gradually increased until 14:00; after this point, they gradually minimized.

Figures 12 and 13 present the CFD and the experimental results of the outlet airflow temperature and the outlet airflow relative humidity, respectively, for the FPSAH models. According to Figures 10 and 11, the results indicate similar trends and a good agreement between the CFD-simulated and experimental results for the outlet air temperature and the outlet airflow relative humidity all over the tested days (the maximum errors were estimated to be 5.6% and 8.2% for the temperature and relative humidity, respectively). The small deviations between the predicted CFD results and the experimental data were explained by the fact of that ANSYS FLUENT takes the ideal characteristics for galvanized iron and glass covers and not their real properties. Additionally, the most likely cause for the deviation was that values of global irradiation used in the CFD simulation were higher than the experimental measured values, as suggested by Figure 7. From these figures, it can also be seen that when temperature increased, the relative humidity decreased. This is because colder air does not require as much moisture to become saturated as warmer air.

The contours of the airflow velocities inside the gap of the two tested FPSAHs, Case A and Case B, at various time intervals throughout the daytime are drawn Figure 14. Figure 14 shows clearly that the high-velocity airflow zones occur in the central section, at the outlet of the tested SAHs. Near the walls (the absorber and glass covers), the velocities are minimized. Additionally, it can be seen from the figure the outlet velocity for Case B was higher than the outlet velocity for Case A for the different time intervals; this is because of the higher temperature values of the SAH's inner the gap, which led to a decrease in the density and therefore an increase in the velocity for a similar mass flow rate. The magnitudes of the velocities are in m/s. Furthermore, the predicted contours of the velocity profile for the tested modified solar air heater (Case B) agreed with the measured velocity inside the stagnant air gab, which measured by calibrated hot-wire anemometers at different positions along the gap section, as can be seen in Figure 2, by making a small hole in the right side of the glass wall and inserting the sensing element (sensor) of the hot-wire anemometer to measure the airflow velocities. We used the silicon rubber to ensure there was no leakage through these holes and the inserted hot-wire anemometers. From the experimental results, the recorded velocities were very small, near to zero.

(Case A) Temperature contour at 10:00. (Case B)

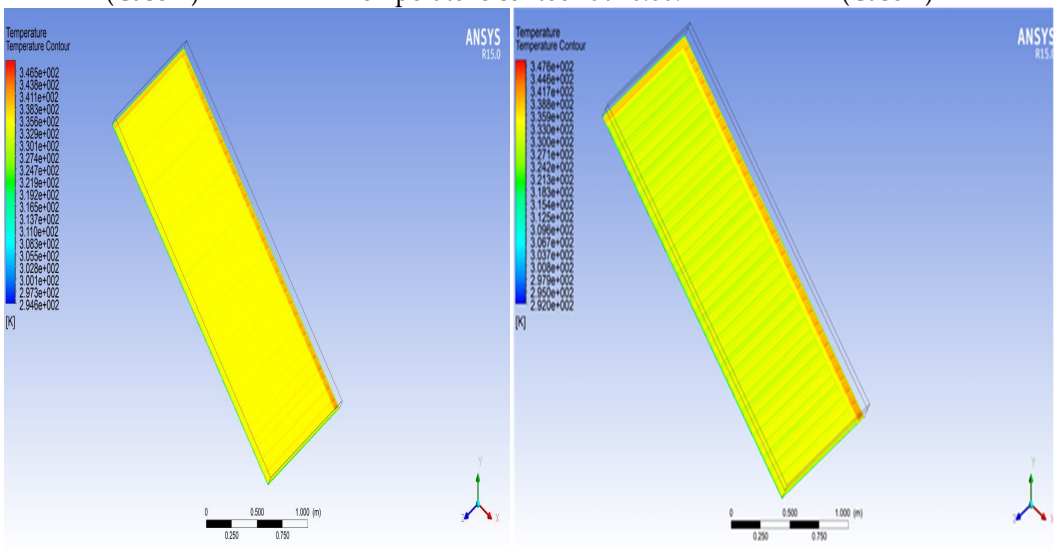

(Case A) Temperature contour at noon. (Case B)

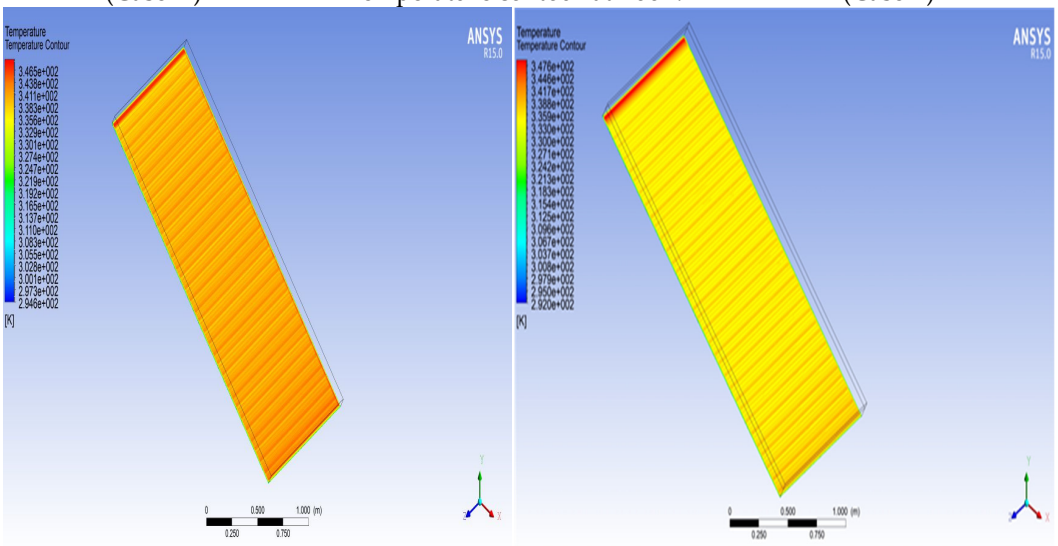

(Case A) Temperature contour at 14:00. (Case B)

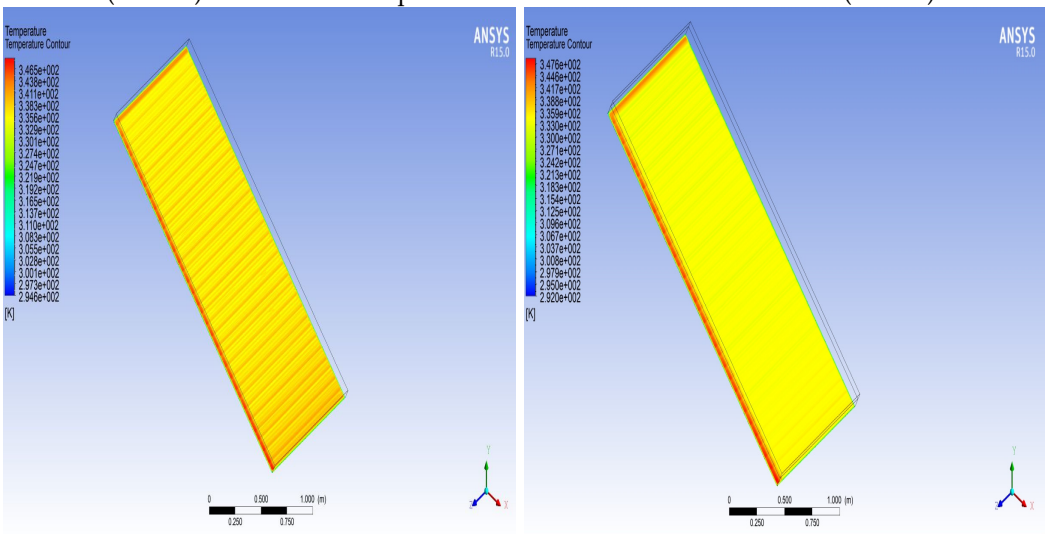

Figure 10. *Cont.*

(Case A) Temperature contour at 16:00. (Case B)

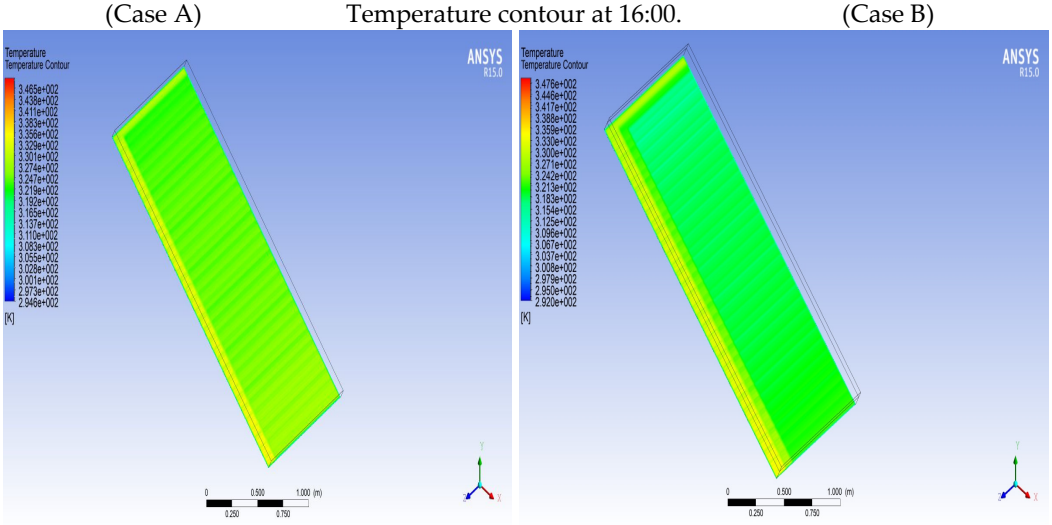

Figure 10. The absorber flat-plate temperature contours at various time intervals.

(Case A) Temperature contour at 10:00 (Case B)

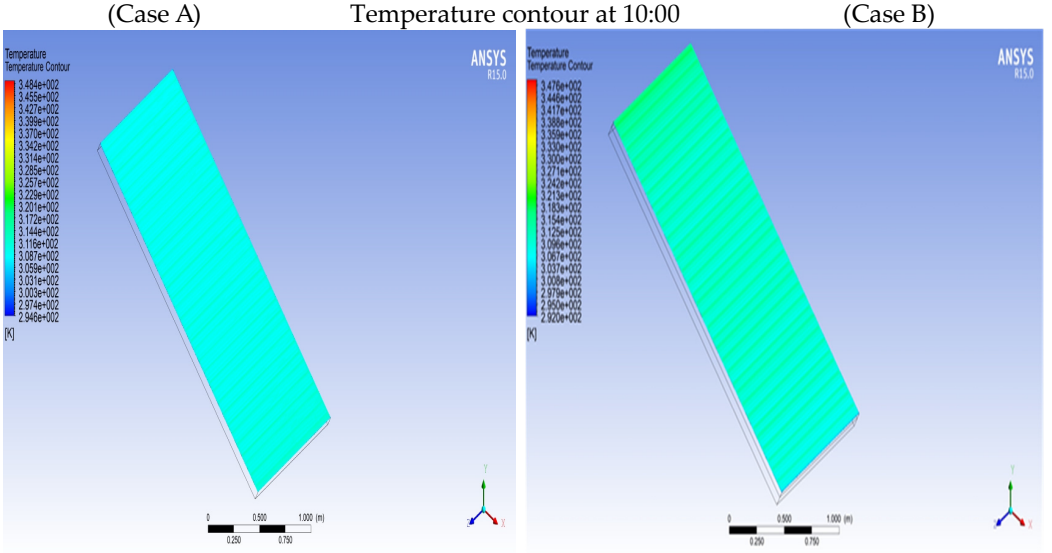

(Case A) Temperature contour at noon. (Case B)

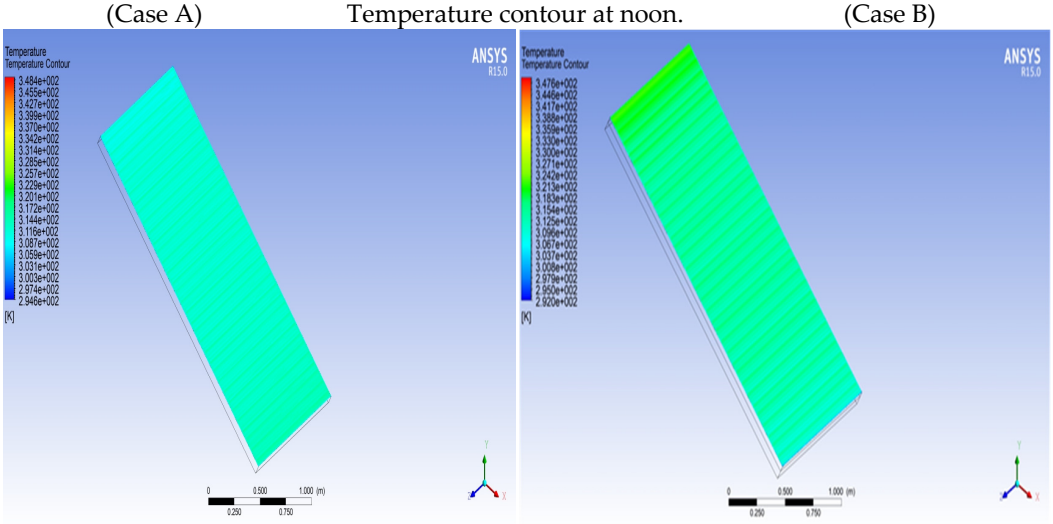

Figure 11. *Cont.*

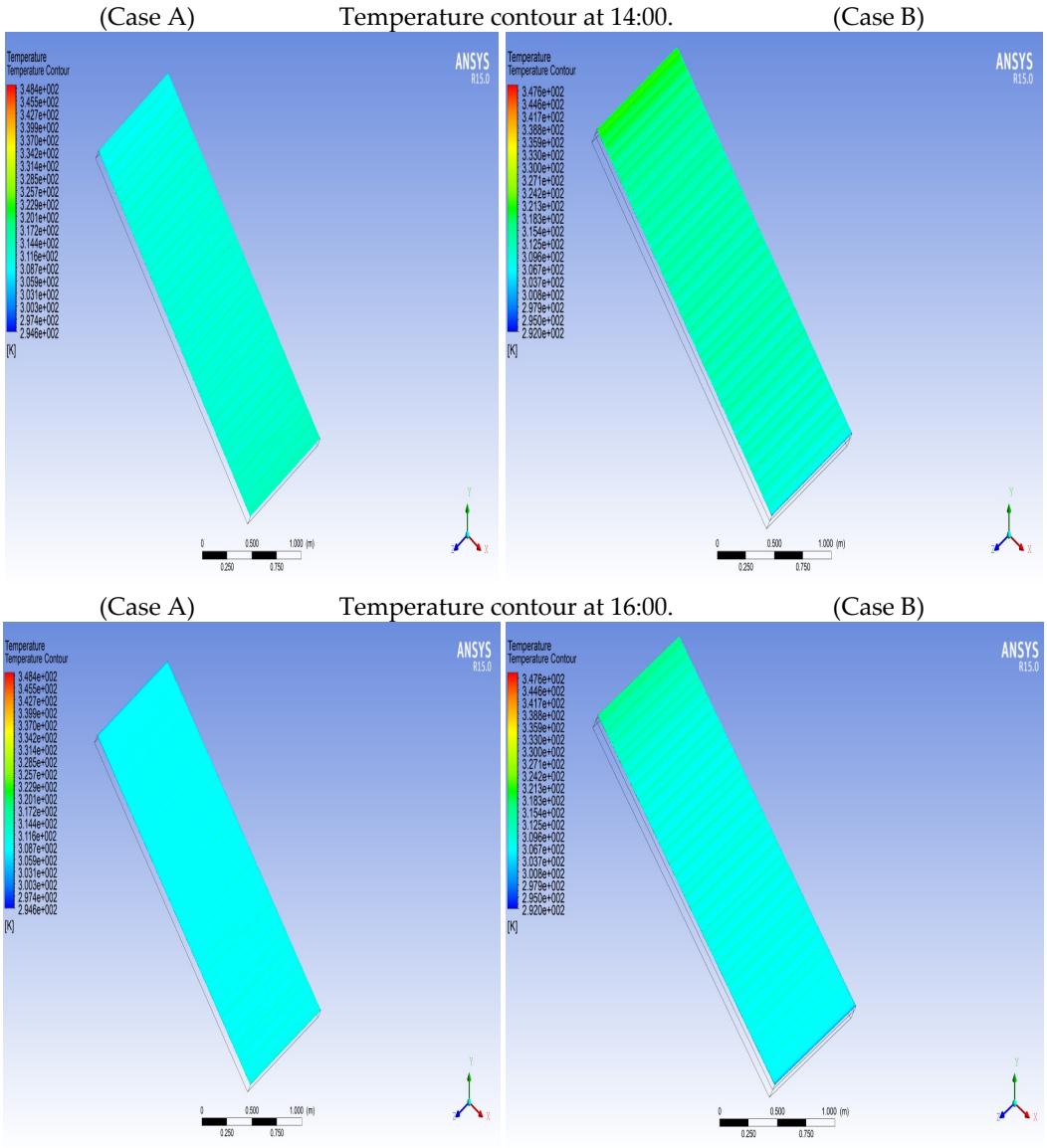

Figure 11. The temperature contours of the upper glass cover at various time intervals.

Figures 15 and 16 indicate the comparison between the CFD simulation and the experimental results of the airflow temperature and the relative humidity inside the two tested SAHs (Case A and Case B) at different time intervals and in different positions on 15 June 2022. In general, there were similar trends and a good agreement between the CFD-simulated and experimental results at the different time intervals and different positions (the maximum errors were estimated to be 4.3% and 7.5% for the temperature and relative humidity, respectively). In addition, the airflow was heated for both tested solar heaters as it traversed along the SAH. The temperature flux increased and decreased with the solar irradiation. Solar air heaters also help to decrease the relative humidity during the day. This is important in the application of SAHs, such as in solar drying, because the reduction in the relative humidity of drying air increases the capacity to absorb humidity from the dried products. From Figures 15 and 16, it can be noted that Case B helped to maintain higher airflow temperatures and a lower airflow relative humidity compared to Case A for the various time intervals and different positions.

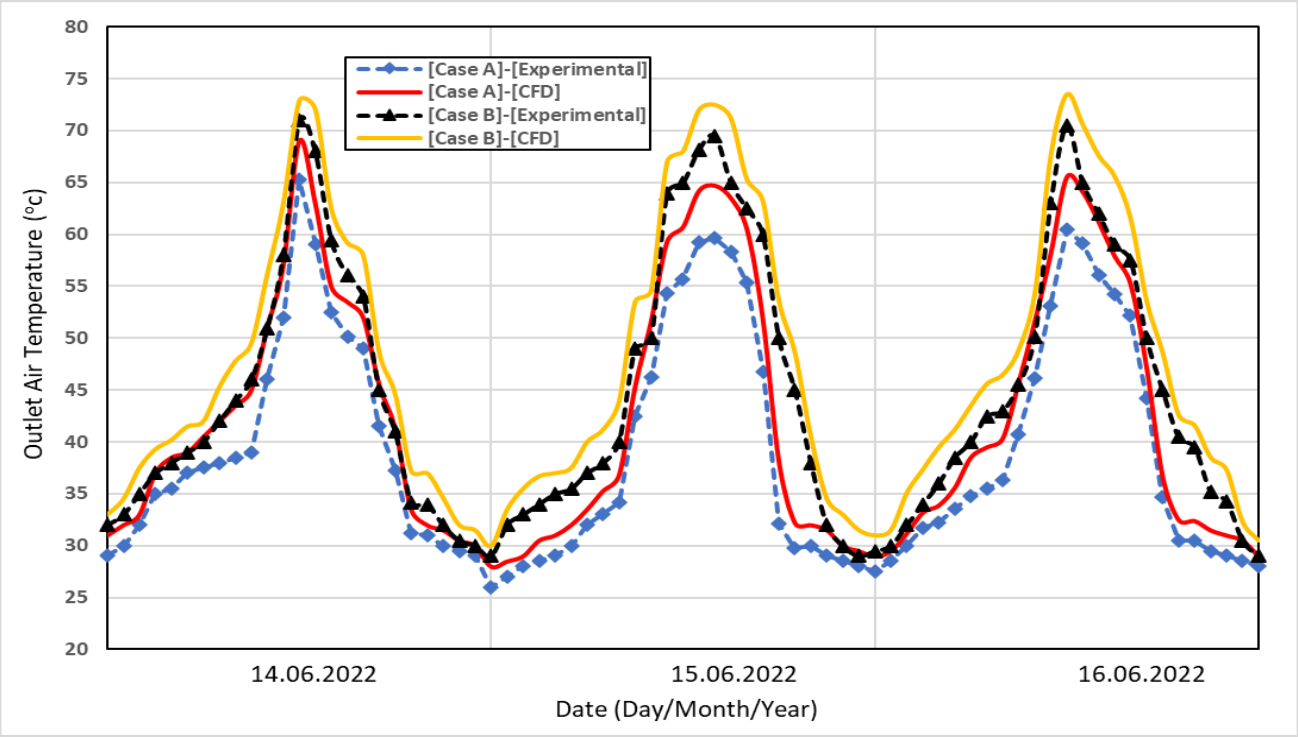

Figure 12. Validation in the CFD outlet airflow temperature variation and the experimental data for the two tested FPSAHs.

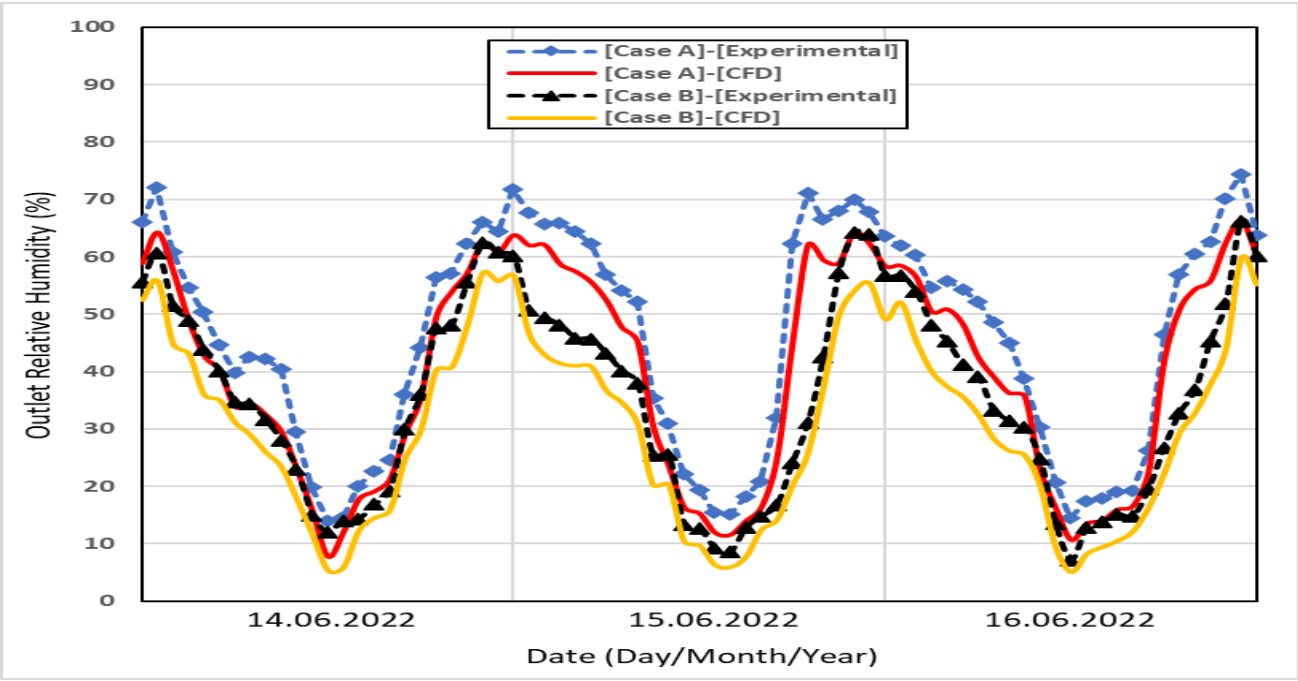

Figure 13. Validation of the CFD outlet airflow relative humidity variation and the experiment data for the two tested FPSAHs.

Figures 17–19 present the CFD and the experimental results of the airflow velocities and the CFD simulation results of the density and pressure ratio along the two tested air heaters (Case A and Case B), respectively, for different time intervals and different positions for 15 June 2022 at 10:00 AM; 1:00 PM, and 4:00 PM. Due to the airflow being heated along with the FPSAH, the density decreased. However, this decrease was due to increased values of solar irradiation. The velocity of the airflow increased along with the FPSAH, but this increase was very low. Depending on the increase, the pressure ratio of the airflow decreased along with the two tested solar air heaters, as indicated in Figure 19.

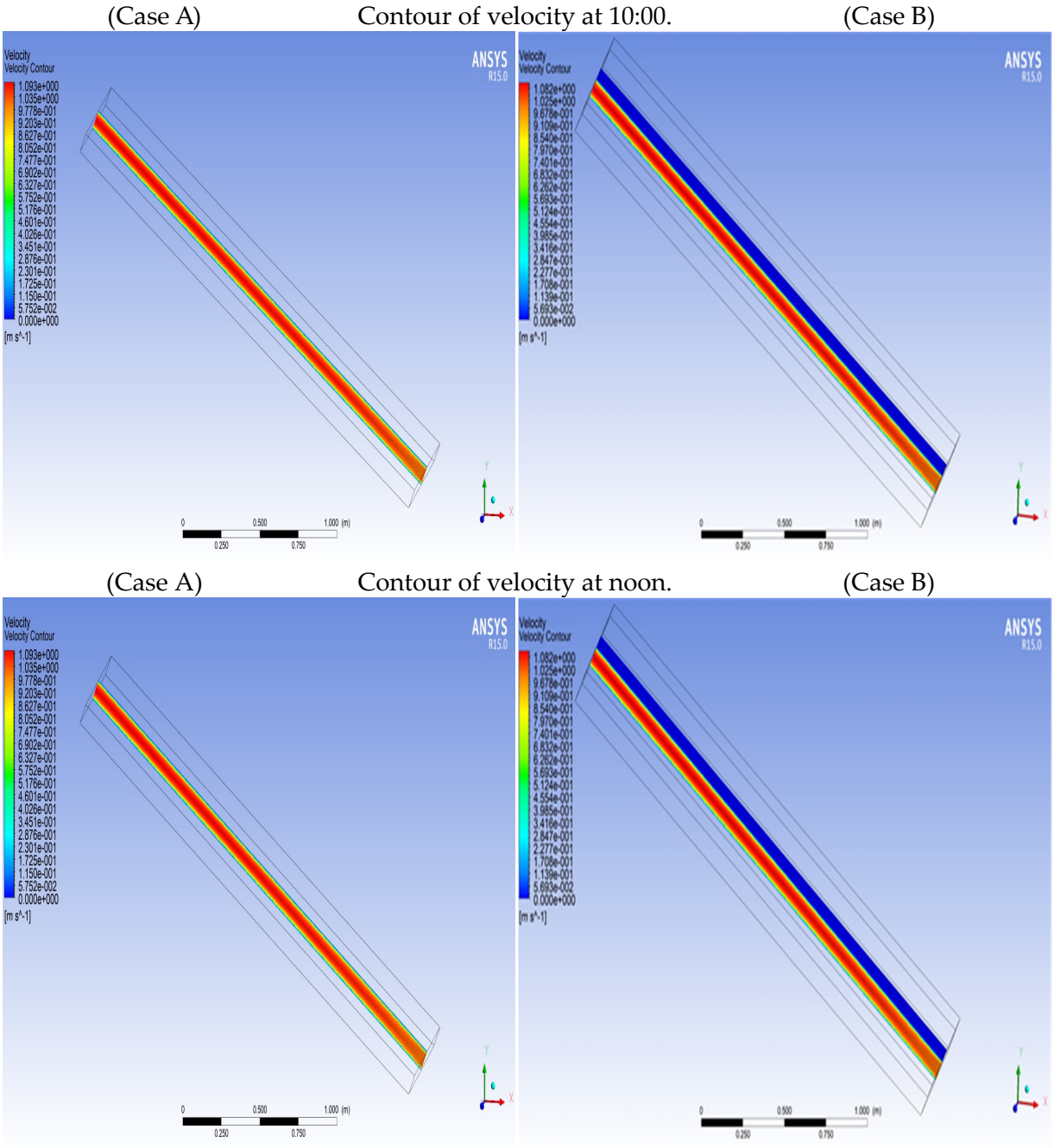

Figure 14. *Cont.*

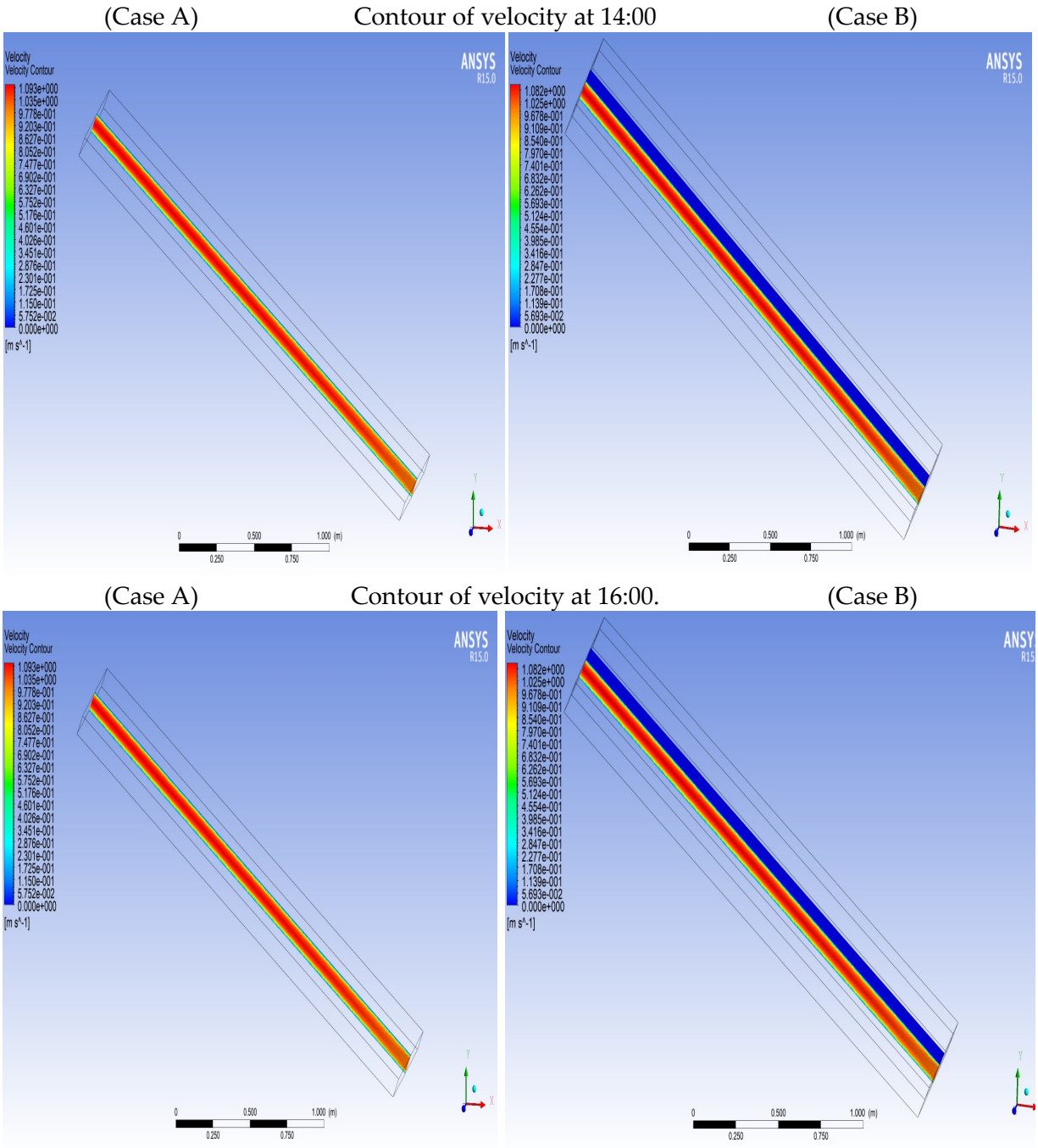

Figure 14. Airflow velocity contours for the tested FPSAHs at various time intervals.

The heating levelized cost (HLC) can be utilized to compare the economic performance of the tested and modified FPSAH (Case B) with the conventional case (Case A) delivering hot air in the desired temperature range. It was computed for all types of cost, such as the capital investment, operating cost, maintenance cost, and inflation rate, etc. The HLC is the parameter that expresses the cost per kWh. It directly relates the cost involved and the thermal performance of the FPSAH. The average lifetime of the two tested FPSAHs was considered to be 20 years. For the modified FPSAH (Case B), the cost per kWh to deliver hot air in the range of 70 to 80 °C is estimated at USD 0.0837, while for the conventional FPSAH (Case A), delivering hot air in the range of 60 to 70 °C, the cost per kWh was estimated at USD 0.0974 for the same tested inlet mass flow rates.

Figures 20–22 present the CFD and experimental values for the average thermal efficiency, average outlet air temperatures and average relative air humidity during the sunny period of the experiment, from 7:00 AM to 7:00 PM, on 16 June 2022. From Figure 20, it can be seen that the average CFD and experimental thermal efficiency values for Case B were higher than that of Case A. The average CFD thermal efficiency values obtained for Case B and Case A were 28.7% and 21.6%, respectively, while the experimental thermal efficiency values for the two cases were 26.4% and 18.2%, respectively. Thus, Case B offers the best thermal efficiency. In addition, from Figure 21, it is clear that the average CFD outlet air temperature values were very close to the experimental results, with deviations of 7% and 7.8% for Case B and the Case A, respectively. Furthermore, from Figure 22, it can be seen that the CFD-simulated average relative humidity was reduced by 31.6% when using case B compared with case A, and reduced by 28.8% for the experimental data compared to Case B.

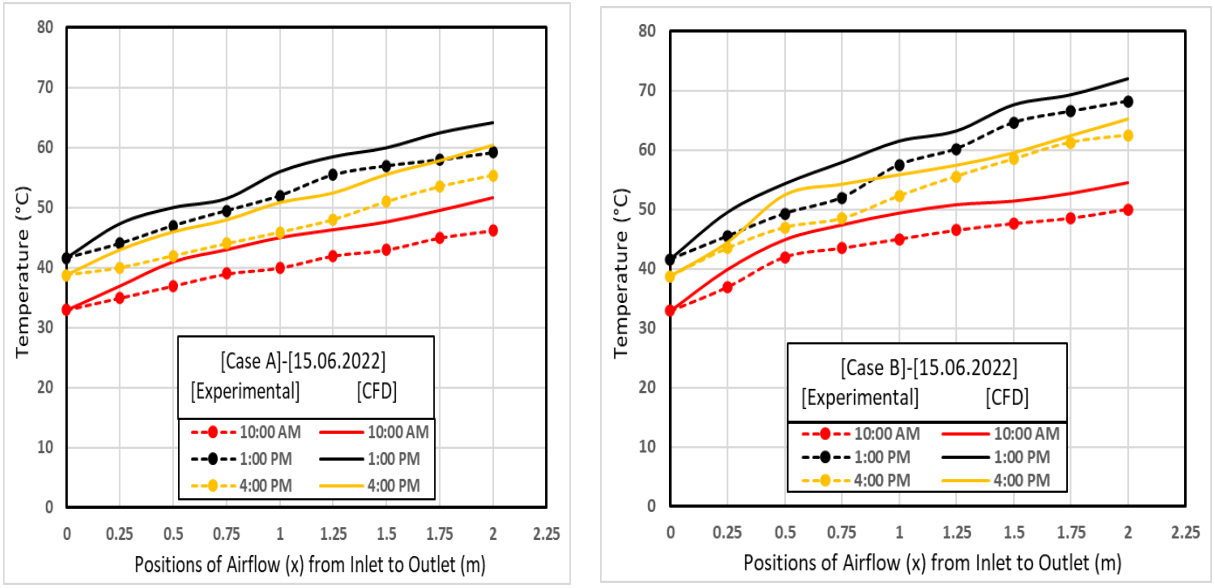

Figure 15. Validation of the CFD airflow temperatures variation and the experimental data for the Case A and Case B FPSAHs tested at various time intervals.

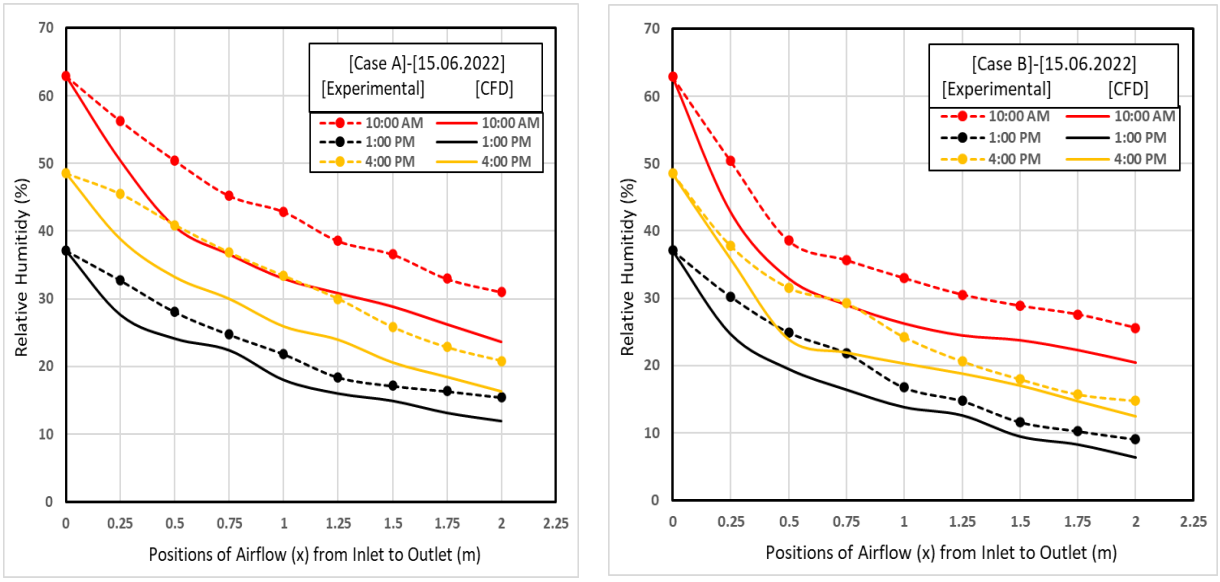

Figure 16. CFD validation of the airflow's relative humidity variation and the experimental data for the Case A and Case B FPSAHs tested at various time intervals.

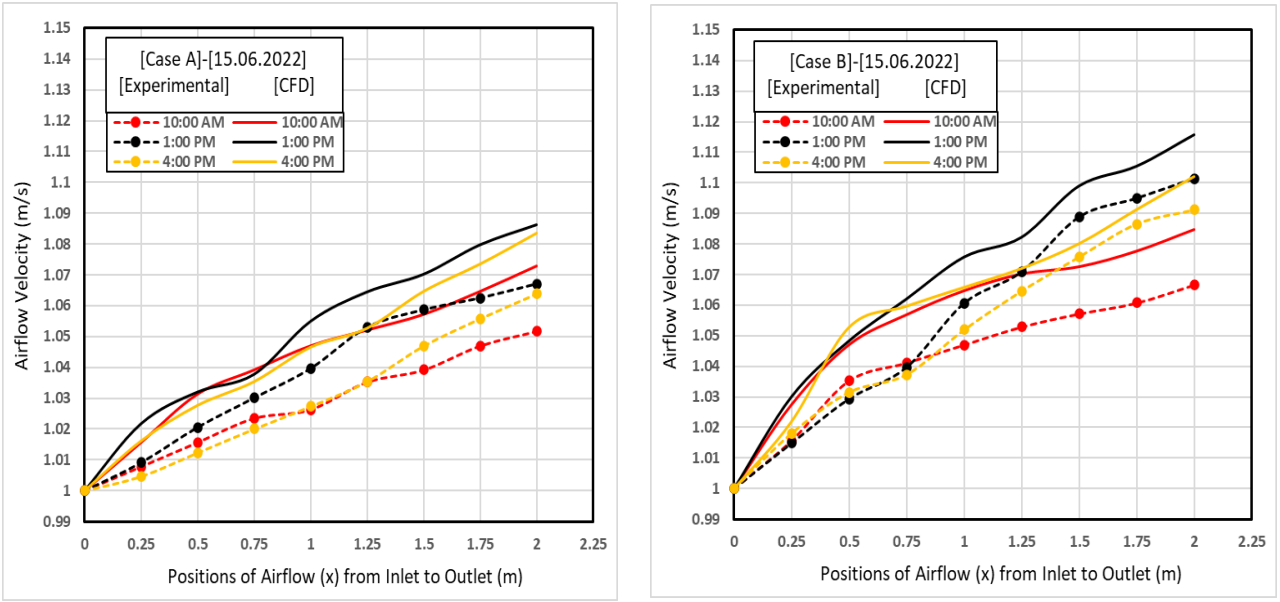

Figure 17. Validation of the variation in the CFD airflow velocity and the experimental data for the Case A and Case B FPSAHs tested at various time intervals.

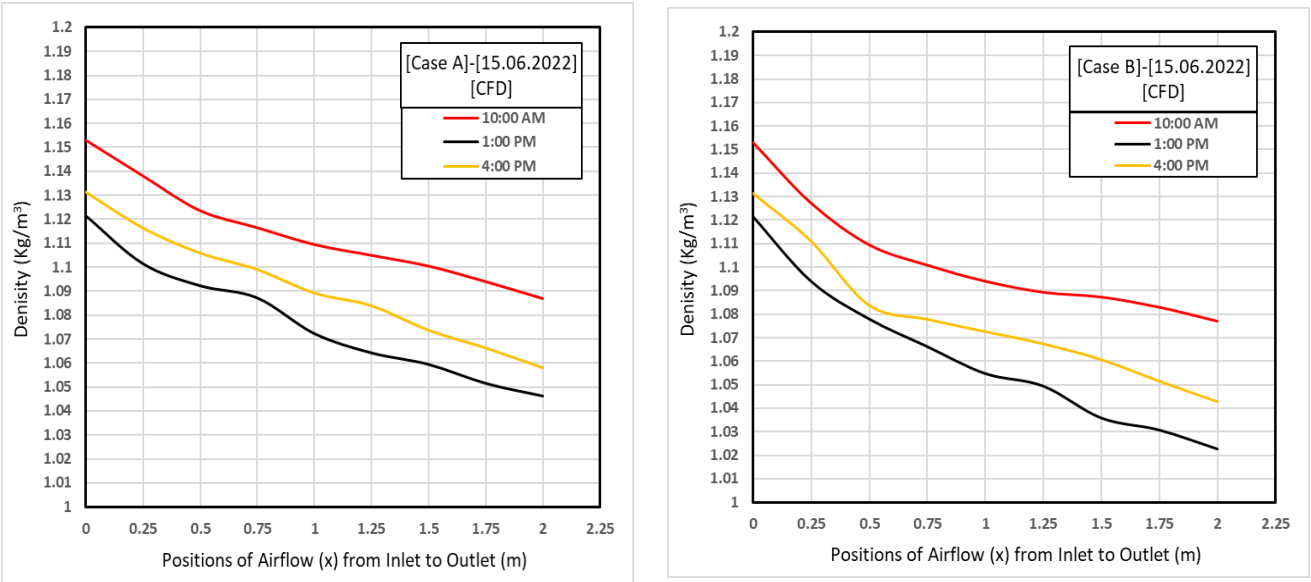

Figure 18. CFD airflow density results for the Case A and Case B FPSAHs tested at various time intervals.

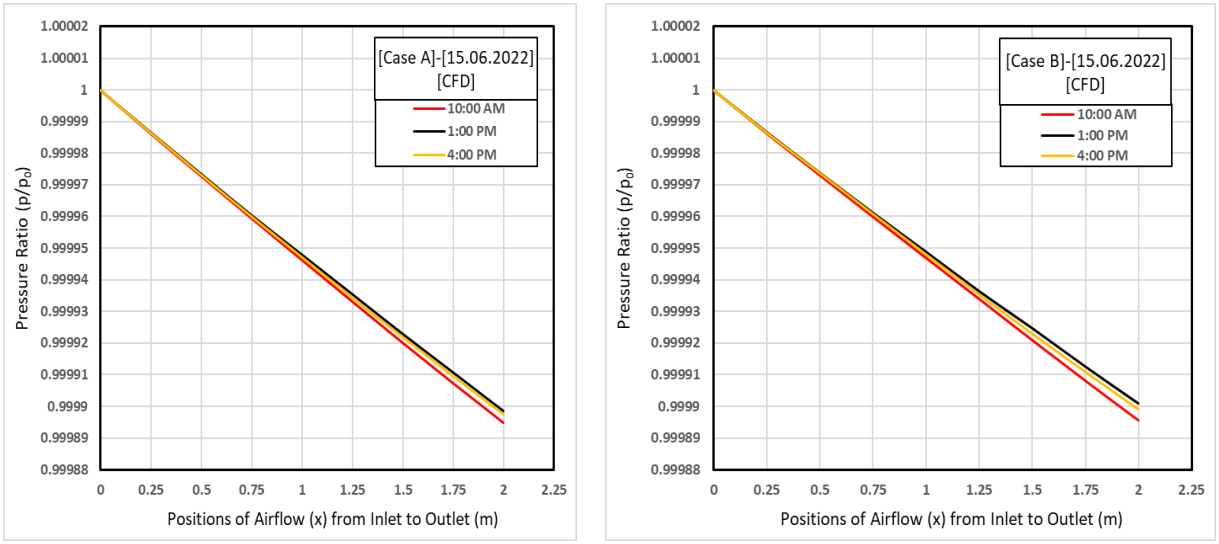

Figure 19. CFD airflow pressure ratio results for the Case A and Case B FPSAHs tested at various time intervals.

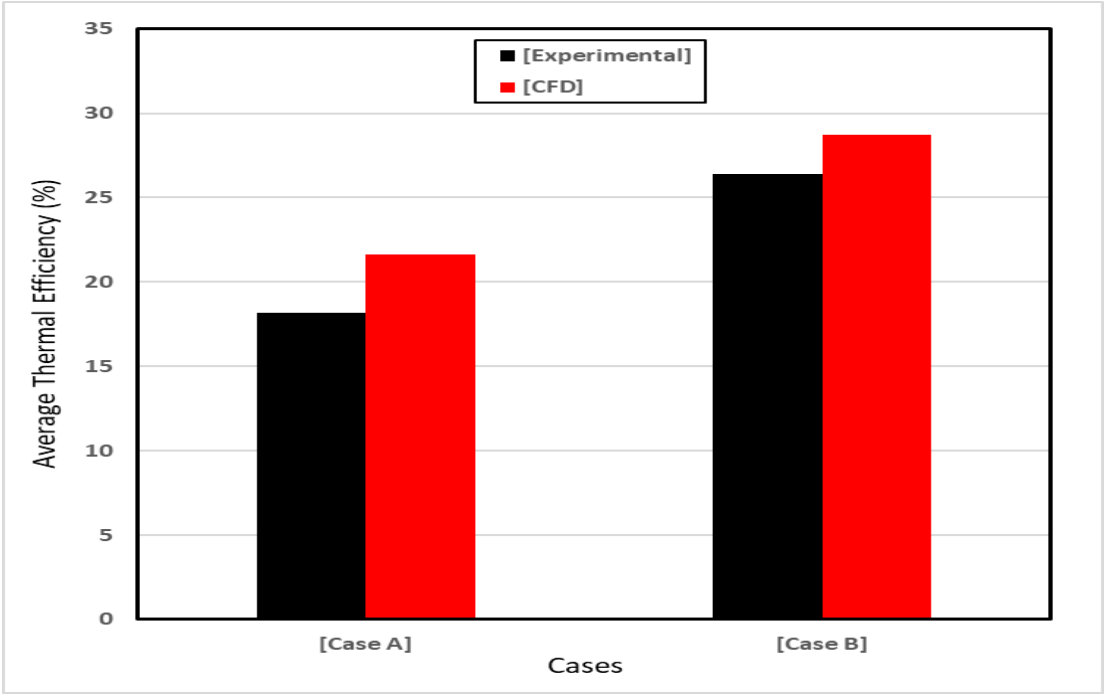

Figure 20. Simulated and experimental average thermal efficiency during the experimental period for the tested Case A and Case B FPSAHs.

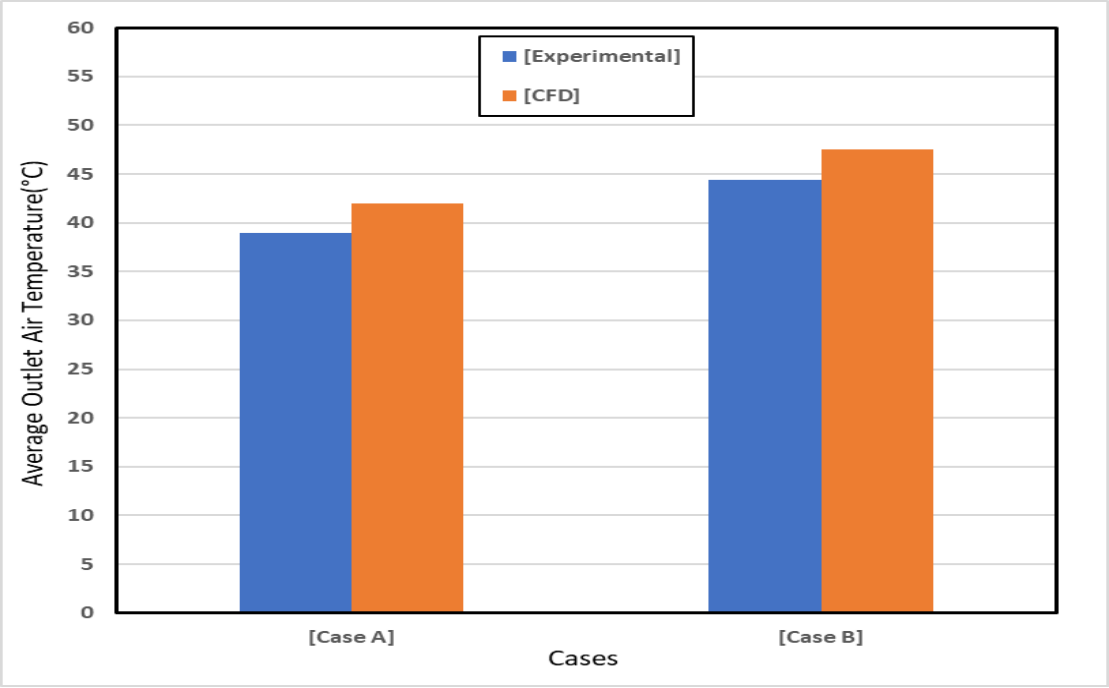

Figure 21. Simulated and experimental average outlet air temperature during the experimental period for the tested Case A and Case B FPSAHs.

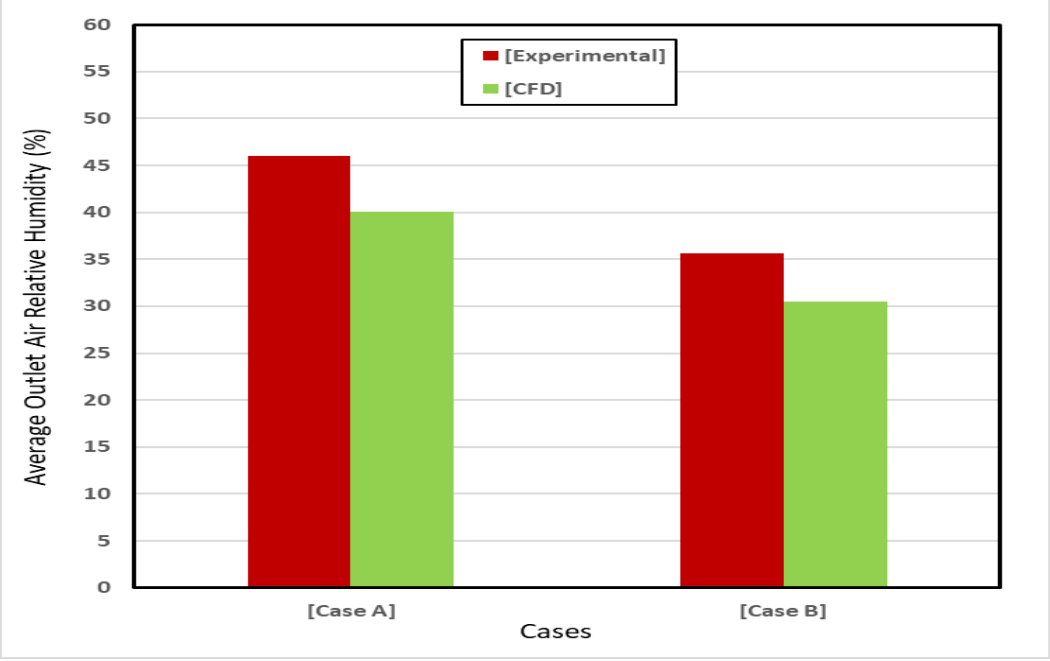

Figure 22. Simulated and experimental average relative air humidity during the experimental period for the tested Case A and Case B FPSAHs.

7. Conclusions

The primary objective of this research was to design and manufacture two distinct models of SAH (conventional—Case A and modified—Case B) and develop a comprehensive three-dimensional CFD model to simulate the performance of the proposed FPSAHs. The conclusions drawn from the CFD simulations and experimental results of this research are as follows:

1. The presence of stagnant air has a beneficial effect on the thermal efficiency of an SAH.
2. CFD simulations provide solutions of satisfactory quality, demonstrating the effectiveness of CFD as a tool for predicting the behavior and performance of FPSAHs.
3. Upon comparison of the CFD-simulated results with the experimental data for both tested SAHs (Case A and Case B), it was observed that the simulated global irradiation, air flow temperature, relative humidity, absorber and glass cover temperatures, and air flow velocities closely matched the corresponding experimental data.
4. The average CFD thermal efficiency values obtained for Case B and Case A were 28.7% and 21.6%, respectively. Meanwhile, the average experimental thermal efficiency values for these cases were 26.4% and 18.2%, respectively. Therefore, it can be concluded that Case B offers the best thermal efficiency.
5. For both Case B and Case A, the average CFD outlet air temperature values demonstrated deviations of 7% and 7.8%, respectively, which were very similar to the corresponding experimental results.
6. Comparing Case B to Case A, the CFD simulation showed a 31.6% reduction in the average relative humidity, while the experimental data exhibited a 28.8% reduction in the relative humidity for Case B compared to the reference case.
7. By conducting a CFD modeling study, designers of FPSAHs can obtain a broad range of efficient information which can help save costs and time before undertaking any expensive and time-consuming experimental investigations.

8. Future Studies

The performance of more complex designs for a solar air heater can be investigated with the help of the presented CFD modeling development approach.

Author Contributions: Designing and manufacturing the experimental setup, performing the CFD simulation, conceptualization, methodology, analyzing the results and writing the original draft, M.S.E.-S.; analysis of the achieved data, cooperating in the scientific discussion and supervision, A.E.; analysis of the achieved data and preparing for the design of the experiments, S.S.E.-D.; validation and contribution to the scientific discussion, F.A.E. All authors have read and agreed to the published version of the manuscript.

Funding: This research received no external funding.

Data Availability Statement: Data may be requested from the corresponding author.

Conflicts of Interest: The authors declare no conflict of interest.

Nomenclature

Variable	Definition	Unit
A_{ab}	Absorber area	m^2
A_{gc}	Glass cover area	m^2
A_{st}	Stagnant air area	m^2
C_{pgc}	The glass cover specific heat	J/kg·K
C_{pst}	The stagnant air specific heat	J/kg·K
C_{pab}	The absorber specific heat	J/kg·K
C_{pf}	The airflow specific heat	J/kg·K
E	The total energy	J
$\vec{g}$	Gravitational acceleration	m/s^2
$h_{cf\text{-}ab}$	The convective coefficient of the heat transfer between the airflow and absorber	$W/m^2 \cdot K$
$h_{cf\text{-}gcu}$	The convective coefficient of the heat transfer between the airflow and the upper glass cover	$W/m^2 \cdot K$
$h_{cgcl\text{-}st}$	The convective coefficient of heat transfer between the lower glass cover and the stagnant air	$W/m^2 \cdot K$

$h_{cgcu\text{-}st}$	The convective coefficient of heat transfer between the upper glass cover and the stagnant air	$W/m^2 \cdot K$
$h_{rgcl\text{-}gcu}$	The radiative coefficient of heat transfer between the lower glass cover and the upper glass cover	$W/m^2 \cdot K$
$h_{rgcl\text{-}sky}$	The radiative coefficient of heat transfer between the lower glass cover and the sky	$W/m^2 \cdot K$
$h_{rgcu\text{-}ab}$	The radiative coefficient of heat transfer between the upper glass cover and the absorber	$W/m^2 \cdot K$
$h_{rab\text{-}gcu}$	The radiative coefficient of heat transfer between the absorber and the upper glass cover	$W/m^2 \cdot K$
$h_{rgcu\text{-}gcl}$	The radiative coefficient of heat transfer between the upper glass cover and the lower glass cover	$W/m^2 \cdot K$
I(t)	Global solar irradiation on the inclined surface	W/m^2
m_{gc}	Mass of glass cover	kg
I	The unit tensor	–
$\vec{j}_j$	The diffusion flux of species j	–
k	The thermal conductivity	W/m.K
m_{st}	Mass of stagnant air	kg
m_{ab}	Mass of absorber	kg
P	The static pressure	Pa
Pr_t	The turbulent Prandtl numbers.	–
S_Q	Volumetric convective thermal power exchanged between airflow and near component	W/m^3
S.L	The volume of airflow located between insulation plate and absorber	m^3
T_{ab}	The absorber temperature	K
T_f	The airflow temperature	K
T_{gcl}	The lower glass cover temperature	K
T_{gcu}	The upper glass cover temperature	K
T_{sky}	The sky temperature	K
T_{st}	The stagnant air temperature	K
T_{amb}	The ambient air temperature	K
T_{fout}	The outlet airflow	K
T_{fint}	The inlet airflow	K
τ_{st}	The stagnant air transmissivity coefficient	–
τ_{gc}	The glass cover transmissivity coefficient	–
τ_f	The airflow transmissivity coefficient	–
α_f	The airflow absorptivity coefficient	–
α_{gc}	The glass cover absorptivity coefficient	–
α_{ab}	The absorber absorptivity coefficient	–
α_{st}	The stagnant air absorptivity coefficient	–
$\vec{V}$	Overall velocity vector	m/s
$\bar{\bar{\tau}}$	The viscous stress	Pa
μ	The molecular viscosity	Pa·s
μ_t	The turbulent viscosity	Pa·s

Abbreviations

Case A	Conventional Solar Air Heater
Case B	Modified Solar Air Heater
CFD	Computational Fluid Dynamics
FPSAH	Flat Plate Solar Air Heater
SAH	Solar Air Heater

References

1. Li, S.; Wang, H.; Meng, X.; Wei, X. Comparative study on the performance of a new solar air collector with different surface shapes. *Appl. Therm. Eng.* **2017**, *114*, 639–644. [CrossRef]
2. Yadav, S.; Saini, R.P. Numerical investigation on the performance of a solar air heater using jet impingement with absorber plate. *Sol. Energy* **2020**, *208*, 236–248. [CrossRef]

3. El-Sebaey, M.S.; Mousavi, S.M.T.; El-Din, S.S.; Essa, F.A. An experimental case study on development the design and the performance of indirect solar dryer type for drying bananas. *Sol. Energy* **2023**, *255*, 50–59. [CrossRef]
4. Akhbari, M.; Rahimi, A.; Hatamipour, M.S. Modeling and Experimental Study of a Triangular Channel Solar Air Heater. *Appl. Therm. Eng.* **2020**, *170*, 114902. [CrossRef]
5. Manjunath, M.S.; Vasudeva Karanth, K.; Yagnesh Sharma, N. Numerical analysis of flat plate solar air heater integrated with an array of pin fins on absorber plate for enhancement in thermal performance. *J. Sol. Energy Eng.* **2019**, *141*, 051008. [CrossRef]
6. Jouybari, N.F.; Lundström, T.S. Performance improvement of a solar air heater by covering the absorber plate with a thin porous material. *Energy* **2020**, *190*, 116437. [CrossRef]
7. Jiaa, B.; Liua, F.; Wang, D. Experimental study on the performance of spiral solar air heater. *Sol. Energy* **2020**, *208*, 236–248. [CrossRef]
8. Wanga, D.; Liua, J.; Liua, Y.; Wanga, Y.; Lib, B.; Liua, J. Evaluation of the performance of an improved solar air heater with "S" shaped ribs with gap. *Sol. Energy* **2020**, *195*, 89–101. [CrossRef]
9. Ojike, O.; Okonkwo, W.I. Study of a passive solar air heater using palm oil and paraffin as storage media. *Case Stud. Therm. Eng.* **2019**, *13*, 100373. [CrossRef]
10. Lakshmia, D.V.N.; Layekb, A.; Kumarc, P.M. Performance analysis of trapezoidal corrugated solar air heater with sensible heat storage material. *Energy Procedia* **2017**, *109*, 463–470. [CrossRef]
11. Kalash, A.R.; Jary, A.M.; Jabe, H.J.; Habeeb, L.J. Implementation of flat plate solar collector design of different design conditions. *J. Mech. Eng. Res. Dev.* **2020**, *44*, 09–26.
12. Chabane, F.; Moummi, N.; Bensahal, D.; Brima, A. Heat Transfer Coefficient and Thermal Losses of Solar Collector and Nusselt Number Correlation for Rectangular Solar Air Heater Duct with Longitudinal Fins Hold under the Absorber Plate. *Appl. Sol. Energy* **2014**, *50*, 19–26. [CrossRef]
13. Moraveja, M. An experimental study of the performance of a solar flat plate collector with triangular geometry. *J. Sol. Energy Res.* **2021**, *6*, 923–936.
14. Shetty, S.P.; Madhwesh, N.; Karanth, K.V. Numerical analysis of a solar air heater with circular perforated absorber plate. *Sol. Energy* **2021**, *215*, 416–433. [CrossRef]
15. Mousavi, S.M.T.; Egelioglu, F. Experimental study of the effect of slit width and slit spacing on the thermal performance of slit-glazed collectors. *Adv. Mech. Eng.* **2017**, *9*, 168781401772847. [CrossRef]
16. Khoukhi, M.; Maruyama, S. Theoretical approach of a flat plate solar collector with clear and low-iron glass covers taking into account the spectral absorption and emission within glass covers layer. *Renew. Energy* **2005**, *30*, 1177–1194. [CrossRef]
17. Abo-Elfadl, S.; Hassan, H.; El-Dosoky, M.F. Study of the performance of double pass solar air heater of a new designed absorber: An experimental work. *Sol. Energy* **2020**, *198*, 479–489. [CrossRef]
18. Nemś, M.; Kasperski, J. Experimental investigation of concentrated solar air-heater with internal multiple-fin array. *Renew. Energy* **2016**, *97*, 722–730. [CrossRef]
19. Khanlari, A.; Güler, H.Ö.; Tuncer, A.D.; Şirin, C.; Bilge, Y.C.; Yılmaz, Y.; Güngör, A. Experimental and numerical study of the effect of integrating plus-shaped perforated baffles to solar air collector in drying application. *Renew. Energy* **2020**, *145*, 1677–1692. [CrossRef]
20. Zhang, H.; Ma, X.; You, S.; Wang, Y.; Zheng, X.; Ye, T.; Zheng, W.; Wei, S. Mathematical modelling and performance analysis of a solar air collector with slit-perforated corrugated plate. *Sol. Energy* **2018**, *167*, 147–157. [CrossRef]
21. Sharma, S.K.; Kalamkar, V.R. Experimental and numerical investigation of forced convective heat transfer in solar air heater with thin ribs. *Sol. Energy* **2017**, *147*, 277–291. [CrossRef]
22. Jin, D.; Quan, S.; Zuo, J.; Xu, S. Numerical investigation of heat transfer enhancement in a solar air heater roughened by multiple V-shaped ribs. *Renew. Energy* **2019**, *134*, 78–88. [CrossRef]
23. Pérez-Espinosa, R.; García-Valladares, O.; Pilatowsky, I. Numerical Modeling and Experimental Validation of Back-Pass Rectangular Ducts Solar Air Heaters. *Appl. Therm. Eng.* **2020**, *171*, 115018. [CrossRef]
24. Relative Humidity Calculator. Available online: https://www.1728.org/relhum.htm (accessed on 12 January 2023).
25. Sureandhar, G.; Srinivasan, G.; Muthukumar, P.; Senthilmurugan, S. Investigation of thermal performance in a solar air heater having variable arc ribbed fin configuration. *Sustain. Energy Technol. Assess.* **2022**, *52*, 102069. [CrossRef]
26. Abuşka, M.; Şevik, S. Energy, exergy, economic and environmental (4E) analyses of flat-plate and V-groove solar air collectors based on aluminium and copper. *Sol. Energy* **2017**, *158*, 259–277. [CrossRef]
27. El-Sebaey, M.S.; Ellman, A.; Hegazy, A.; Ghonim, T. Experimental Analysis and CFD Modeling for Conventional Basin-Type Solar Still. *Energies* **2020**, *13*, 5734. [CrossRef]
28. El-Sebaey, M.S.; Hegazy, A.; Ellman, A.; Ghonim, T. Experimental and CFD Study on Single Slope Double Basin Solar Still. *Eng. Res. J.* **2021**, *44*, 21–32. [CrossRef]